energy&fuels

pubs.acs.org/EF

Article

Effects of Flame Conditions on Structure and Methane Oxidation Activity of Pd/$Ce_xZr_{1-x}O_2$ Catalysts

Can Wang, Ben Ko, and Erdem Sasmaz*

Cite This: *Energy Fuels* 2024, 38, 15571−15586

Read Online

ACCESS | Metrics & More | Article Recommendations | Supporting Information

ABSTRACT: Solid solution catalysts doped with Pd can be used to enhance the low-temperature methane oxidation activity by increasing the oxygen storage capacity, metal−support interaction, and oxygen mobility. In this work, we systematically synthesized Pd-doped $Ce_xZr_{1-x}O_2$ solid solution catalysts using flame spray pyrolysis (FSP) as a robust synthesis method to determine the synthesis−structure−activity relationship for methane oxidation. We examined the impact of precursor molarity, liquid feed rate, and oxygen flow rate on the oxygen vacancy percentage (OV%), Pd speciation, and metal−support interaction. Our results indicate that increasing the liquid feed rate or decreasing the oxygen flow rate in FSP results in higher OV% of the Pd/$Ce_xZr_{1-x}O_2$ catalyst. The catalysts with higher OV% have weaker metal−support interaction and promote the formation of peroxide species (O_2^{2-}). A lower precursor molarity leads to the formation of relatively larger PdO nanoparticles, which in turn decreases Pd dispersion. Of particular importance, Pd speciation can be controlled by the equivalence ratio (ER). Catalysts synthesized in ER < 1 favor the formation of incorporated Pd^{2+} species, while mostly finely dispersed PdO nanoparticles can be observed at ER > 1. Finely dispersed PdO nanoparticles in Pd/$Ce_xZr_{1-x}O_2$ exhibit higher turnover frequencies (TOFs) for methane oxidation compared to those with more incorporated Pd^{2+} species. The TOFs at 400 °C of Pd/$Ce_{0.5}Zr_{0.5}O_2$ samples can be adjusted from 0.10 to 0.21 s^{-1} by modifying the synthesis conditions in the FSP, which impacts the OV% and Pd speciation of the catalyst. The enhanced methane oxidation activity is attributed to the synergistic interaction among PdO nanoparticles, oxygen vacancies, and peroxide species.

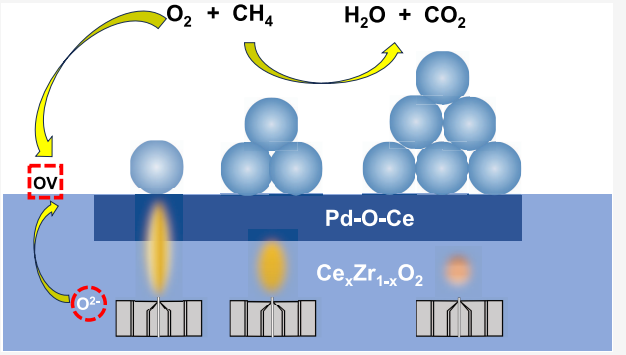

1. INTRODUCTION

Methane is the primary component of natural gas and has the lowest carbon-to-hydrogen ratio among all hydrocarbons. This makes it an attractive energy source for internal combustion engines due to its high gravimetric energy density (55.6 MJ/kg) and low emission of CO_2, particulate matter (PM), and NO_x.[1,2] Despite its benefits in energy density and emissions, unburned methane can slip through catalytic converters during the cold start at low engine temperatures due to its high molecular stability.[3,4]

Pd/CeO_2-based catalysts have gained attention for their methane oxidation at temperatures below 400 °C[4] due to the active oxygen species provided by the Ce redox pairs (Ce^{3+} and Ce^{4+}) at low reaction temperatures.[5−7] Methane oxidation generally follows the Mars−van Kravelin mechanism in which CH_4 first adsorbs and dissociates to CH_3^- on the PdO surface, followed by its oxidation by oxygen from PdO. PdO is reduced to $Pd^{\delta+}$ ($0 < \delta < 2$) and oxidized back to PdO by gas phase O_2 or surface oxygen from the CeO_2 support, generating oxygen vacancies (OVs).[8,9] Hence, CH_4 activation on the PdO species and the redox cycle of PdO species are essential steps for high methane oxidation activity. Incorporating Zr^{4+} ions into the CeO_2 lattice forms a $Ce_xZr_{1-x}O_2$ solid solution and can further enhance oxygen mobility, reducibility, and metal−support interaction, shifting the T_{50} for methane oxidation below 400 °C.[10−14] However, the benefit of Zr incorporation or enhanced Pd interaction with CeO_2-based supports largely depends on the synthesis technique used. Alternative synthesis techniques, such as solvent-thermal and solution-combustion syntheses of Pd/$Ce_xZr_{1-x}O_2$, can show superior methane oxidation activity compared to coprecipitation and impregnation. Pd/$Ce_xZr_{1-x}O_2$ synthesized via a solvent-thermal technique using a block of copolymer followed by aging and calcination for 36 h can form a κ-$Ce_xZr_{1-x}O_2$ phase, which improves the interaction between Pd and support, enhancing oxygen mobility.[15−17] The solution-combustion synthesis can incorporate Pd ions into the $Ce_xZr_{1-x}O_2$ due to the high combustion temperatures, generating undercoordinated oxy-

Received: April 22, 2024
Revised: July 6, 2024
Accepted: July 8, 2024
Published: July 24, 2024

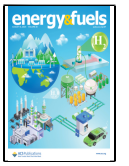

gen atoms and improving the Pd^{2+} redox ability.[15,16] Despite their benefits, these synthesis techniques can be lengthy and produce undesired strong agglomerates. Alternatively, flame spray pyrolysis (FSP) is a robust synthesis that can produce nanoparticles (NPs) at high production rates with the desired particle size,[18,19] crystalline phase,[20,21] OV concentration,[22,23] and morphology.[24,25] To date, only a few articles have reported the performance of flame-made catalysts for methane oxidation, and those mainly focused on the effect of solvents and dopant concentrations on methane oxidation activity.[23,26,27] However, the impact of FSP combustion conditions on PdO redox ability and its interaction with $Ce_xZr_{1-x}O_2$ have not been investigated.

Our study focuses on understanding the synthesis−activity relationship, which is fundamental to enhancing the low-temperature methane oxidation activity of $Pd/Ce_xZr_{1-x}O_2$. We aim to investigate the impact of FSP synthesis conditions on several factors, such as OV formation, metal−support interaction, Pd dispersion, and Pd speciation of $Pd/Ce_xZr_{1-x}O_2$ solid solution catalysts. To achieve this, we have conducted a thorough investigation and characterization of the catalysts, including their crystallinity, phase, oxygen vacancy percentage (OV%), reducibility, and Pd speciation. This comprehensive data is systematically analyzed at different liquid feed rates, oxygen flow rates, equivalence ratios (ERs), and precursor molarity values to investigate the impact of the synthesis conditions on methane oxidation performance.

2. EXPERIMENTAL SECTION

2.1. Catalyst Synthesis. $Pd/Ce_xZr_{1-x}O_2$ (where x = 0.66, 0.5, and 0.33) catalysts were synthesized in an FSP reactor, as shown in Figure 1. Cerium(III) 2-ethylhexanoate (Alfa Aesar, 49% in 2-ethylhexanoic acid, 12% as Ce), zirconium(IV) oxide 2-ethylhexanoate (Alfa Aesar, in mineral spirits, ∼6% as Zr), and palladium(II) acetylacetonate (Sigma-Aldrich, purity = 99%) were used as precursors of Ce, Zr, and Pd, respectively. The specified amounts of each precursor were dissolved in a 1:1 volumetric ratio of 2-ethylhexanoic acid (Sigma-Aldrich, purity ≥ 99%) and toluene (Sigma-Aldrich, anhydrous, purity = 99.8%). The molar ratios of Ce and Zr used in the syntheses were 2:1, 1:1, and 1:2. The total molarity of precursors dissolved in fuel was 0.2, 0.3, and 0.4 M. While the precursors' molarities varied, the Pd content kept constant at 0.8 wt% in all samples. The mixture solution of precursor and fuel was injected through a capillary of a stainless-steel gas-assisted atomizer (Schlick Atomizing Technologies, Germany), dispersed to a fine spray by oxygen dispersion gas, and ignited by CH_4/air flat flame (CH_4: 1 L/min, air: 10 L/min) from the burner (Holthius and Associates, McKenna burner) to produce particles. The liquid injection feed rate was 2 and 3 mL/min (denoted as Lp, where p represents the liquid flow rate) using a syringe pump (New Era Pump Systems Inc., NE-4000). The oxygen gas flow rate was controlled by a mass flow controller (Brooks) at 4−6 L/min (denoted as Oq, where q represents the oxygen flow rate). The pressure drop at the nozzle tip was fixed at 1.5 bar. The particles were collected on Whatman glass microfiber filters (Sigma-Aldrich, grade GF/D, 257 mm in diameter) located above the FSP nozzle using a vacuum pump.

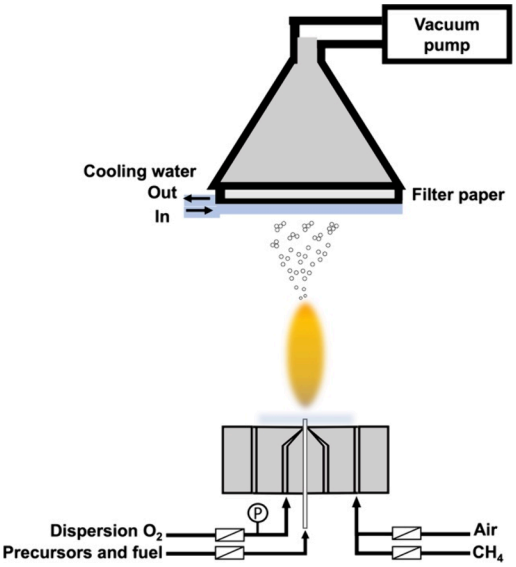

Figure 1. Schematic image of FSP synthesis apparatus.

The equivalence ratio (ER) is defined as the ratio of the actual fuel/air ratio to the stoichiometric fuel/air ratio, as shown in eq 1. The synthesis conditions can be adjusted to the reducing synthesis environment (ER > 1) and oxidizing synthesis environment (ER < 1) by tuning the feed rate of the precursor and fuel mixture and the dispersion gas flow rate.

$$\mathrm{ER} = \frac{\left(\frac{\mathrm{F}}{\mathrm{O}}\right)_{\mathrm{actual}}}{\left(\frac{\mathrm{F}}{\mathrm{O}}\right)_{\mathrm{stoich}}} \quad (1)$$

2.2. Catalyst Characterization. The X-ray diffraction (XRD) patterns of as-synthesized samples were characterized on a LEXI-Rigaku Ultima III powder X-ray diffractometer using Cu Kα radiation (λ= 0.154 nm) and a power of 40 kV × 30 mA. The XRD data were collected over a 2θ range of 20−80° with a scan step size of 0.02° and a scanning speed of 2°/min. Data processing, including background correction and Kα_2 stripping, was accomplished using Rigaku data analysis software. The crystallite size (d) of the samples was determined using the Scherrer equation. The full width at half-maximum (fwhm) of a prominent diffraction peak was corrected for instrumental broadening and used in the Scherrer equation,

$$d = \frac{K\lambda}{\beta \cos\theta} \quad (2)$$

where K is the shape factor (0.9 is used in this work), λ is the X-ray wavelength, β is the corrected fwhm in radians, and θ is the Bragg angle corresponding to the peak position.

The surface areas of the catalysts were determined from Brunauer−Emmett−Teller (BET) isotherms using N_2 adsorption at 78 K. The samples were degassed at 300 °C for 7 h to remove the moisture prior to the measurements. Assuming that the particles are monodispersed and spherical, the equivalent BET particle size (d_{BET}) can be derived from the calculated specific surface area (SSA) by eq 3,

$$d_{\mathrm{BET}} = 6000/\rho \cdot \mathrm{SSA} \quad (3)$$

where d_{BET} is expressed in [nm], SSA is in [m^2/g], and ρ is the density of nanoparticles in [g/cm^3]. The equation assumes that the particles are monodispersed and spherical.

High-angle annular dark-field scanning transmission electron microscopy (HAADF-STEM) images were taken on a JEOL JEM-ARM300F Grand ARM atomic resolution electron microscope at an acceleration voltage of 300 kV. Elemental mapping images were acquired with energy-dispersive X-ray spectroscopy (EDS). The powder sample was ultrasonically dispersed into ethanol, and droplets of the suspensions were deposited onto a holey carbon copper grid for analysis. Up to 74 particles are counted to determine the particle size distribution.

Raman spectra were acquired over a customized optical microscopy platform based on the Renishaw InVia Raman microscope. 532 nm (1.1 mW) has been utilized as the excitation source. Raman spectra were collected in a frequency range of 30−1400 cm^{-1}. Oxygen vacancies of the samples are calculated from the peak fitting using the peak area of the δ and F_{2g} bands as shown in eq 4,

https://doi.org/10.1021/acs.energyfuels.4c01888
Energy Fuels 2024, 38, 15571−15586

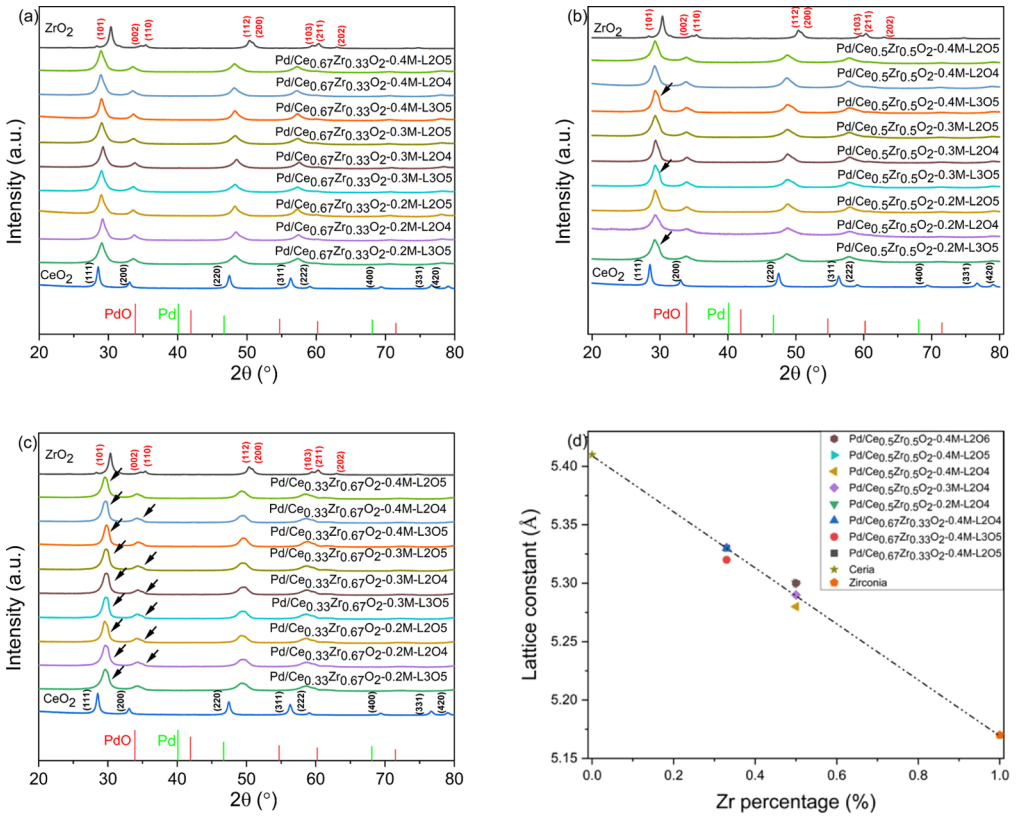

Figure 2. XRD patterns of (a) $Pd/Ce_{0.67}Zr_{0.33}O_2$, (b) $Pd/Ce_{0.5}Zr_{0.5}O_2$, and (c) $Pd/Ce_{0.33}Zr_{0.67}O_2$ samples synthesized at different molarities and oxygen and liquid flow rates. (d) Lattice constant of solid solution samples as a function of Zr percentage (%). Black arrows indicate the tetragonal ZrO_2 phase.

$$\mathrm{OV\%} = \frac{A_{\delta}}{A_{F_{2g}} + A_{ov}} \times 100\% \quad (4)$$

where A_{OV} and $A_{F_{2g}}$ are the areas of the OV peak and the F_{2g} peak, respectively. The method to calculate the error bar of OV% is provided in the Supporting Information.

The H_2 temperature-programmed reduction (TPR) experiments were performed to investigate the surface or/bulk oxygen reduction behaviors of the as-synthesized samples in the temperature range of 30−800 °C, using the 3Flex surface and a catalyst characterization analyzer (Micromeritics). The 50 mg sample, placed in a U-shaped quartz tube, was first thermally treated under a 50 mL/min flow of N_2 at 200 °C for 2 h to remove the adsorbed species on the sample surface and then cooled down to 30 °C. The H_2/Ar mixture (5%) was injected at a flow rate of 50 mL/min. The temperature ramping rate was 10 °C/min. The TPR was recorded by a thermal conductivity detector (TCD). The hydrogen consumption indicated by the reduction peaks was calculated using CuO as the reference.

X-ray photoelectron spectroscopy (XPS) of the catalysts was performed using a Kratos AXIS-Supra instrument equipped with a dual Al Kα/Ag Lα monochromatic X-ray source (2984.2 eV). The alpha hemispherical analyzer was operated in the constant energy mode with survey scan pass energies of 200 eV to measure the whole energy band and 50 eV in a narrow scan to selectively measure the elements. The peak fitting for our data evaluation was processed using CasaXPS software. An estimation of intensities was done after a nonlinear "Shirley-type" background subtraction and fitting the experimental curve to a combination of Gaussian (70%) lines and Lorentzian (30%) lines. Binding energies are calibrated to the C 1s line at 284.6 eV.

Time-resolved in situ diffuse reflectance infrared Fourier transform spectroscopy (DRIFTS) was carried out in a DRIFT cell (Harrick Praying Mantis) using a Fourier transform infrared spectrometer (Bruker VERTEX 70) equipped with a liquid-nitrogen-cooled mercury−cadmium−telluride (MCT) detector. The background spectra were collected prior to introducing the CO. The gas mixture of CO/N_2 (1000 ppm) was then injected at 10 mL/min into the DRIFT cell. Both sample and background spectra were collected for 64 scans with a 4 cm^{-1} resolution.

X-ray absorption spectroscopy (XAS) measurements of the Pd K-edge were conducted in the 10-BM beamline at the Advanced Photon Source (APS). The fluorescence yield mode of the samples was collected using a four-element Vortex detector. Pd metal foil was analyzed in transmission mode as a reference and for monochromatic energy calibration. The percentages of Pd^{2+} and Pd^0 for each sample are determined by linear combination fitting using Athena.[28]

The metal dispersion was calculated through H_2-chemisorption. 100 mg of catalyst was loaded in a U-shaped quartz tube and pretreated in a 50 mL/min flow of H_2 at 400 °C for 1 h. After that, the sample was cooled to 35 °C and purged under Ar for 1 h. 10% H_2/Ar was passed through the sample tube at 35 °C at 5 min intervals until the catalyst was saturated. The active Pd sites were calculated from the adsorbed H_2 volume, assuming a H/Pd stoichiometry factor of 1.[29,30]

The actual Pd concentration was measured using a Thermo Scientific iCAP RQ inductively coupled plasma mass spectrometer (ICP-MS). 5 g of sample was placed into a Teflon vessel, followed by the addition of 40 mL of concentrated nitric acid. The sample was heated to 200 °C at 800 W for 1 h in a microwave oven (CEM MARS6) to obtain a homogeneous solution. The solution was diluted with distilled water to a total volume of 100 mL. After that, additional dilution was prepared with 1% (v/v) nitric acid.

2.3. Catalytic Activity Evaluation of Catalysts. Catalytic activity tests for methane oxidation were carried out in a 4 mm i.d. stainless-steel packed-bed reactor (PBR). 12.5 mg of catalyst powder was placed between quartz wool layers. The inlet feed gas mixture, composed of 0.5% CH_4 and 4% O_2 and balanced with N_2, was injected into the reactor by using mass flow controllers (Brooks

https://doi.org/10.1021/acs.energyfuels.4c01888
Energy Fuels 2024, 38, 15571−15586

Table 1. Equivalence Ratio, Oxygen Vacancy Percentage, Hydrogen Consumption, Pd Content, Pd Dispersion, and the Ratio of Pd^{2+} to Pd^0 in $Pd/Ce_xZr_{1-x}O_2$ Samples[a]

							H_2 consumption (μmol g^{-1})					ratio (%) by XPS			ratio (%) by XANES	
sample	ER	cryst size (nm)	BET surf area (m^2/g)	BET size (nm)	Part size (nm)	OV (%)	α peak	β peak	total of α and β	Pd content (wt%)	Pd disp (%)	Pd^{2+}	Ce^{3+}	OV	Pd^{2+}	Pd^0
$Pd/Ce_{0.5}Zr_{0.5}O_2$ -0.4M-L2O6	0.70	6.11	94.7	9.8	6.2	23.8	56.0	721.5	777.5	0.85	24.7	71.4	20	34.0	79.4	20.6
$Pd/Ce_{0.5}Zr_{0.5}O_2$ -0.4M-L2O5	0.84	7.94	75.1	12.4	8.2	25.1	683.1	77.6	760.7	0.84	25.8	69.9	24	37.5	72.9	27.1
$Pd/Ce_{0.5}Zr_{0.5}O_2$ -0.4M-L2O4	1.05	7.52	82.9	11.2	7.5	27.2	707.4	48.8	756.2	0.79	25.3	65.1	30	38.0	72.4	27.6
$Pd/Ce_{0.5}Zr_{0.5}O_2$ -0.3M-L2O4	1.06	8.08	71.8	13.0	8.0	26.7	566.2	108.7	674.9	0.80	23.9	-	-	-	-	-
$Pd/Ce_{0.5}Zr_{0.5}O_2$-0.2M-L2O4	1.06	8.64	61.4	15.1	8.7	26.3	496.2	183.6	679.8	0.80	18.7	-	-	-	-	-
$Pd/Ce_{0.67}Zr_{0.33}O_2$-0.4M-L2O4	0.96	8.23	75.0	12.4	-	19.9	591.5	75.6	667.1	0.85	26.3	-	-	-	-	-
$Pd/Ce_{0.67}Zr_{0.33}O_2$-0.4M-L3O5	1.14	8.84	77.1	12.1	-	17.7	669.1	0	669.1	0.85	24.2	-	-	-	-	-
$Pd/Ce_{0.67}Zr_{0.33}O_2$-0.4M-L2O5	0.76	7.93	72.0	12.9	-	16.8	98.9	568.3	667.2	0.85	24.0	-	-	-	-	-

[a]Cryst size: the crystallite size of $Pd/Ce_xZr_{1-x}O_2$ calculated from XRD; BET size: equivalent BET particle size calculated from BET surface area; Part size: particle size of $Ce_xZr_{1-x}O_2$ nanoparticles measured from STEM images; Pd disp %: the percentage of Pd dispersion.

Instrument). The weight hourly space velocity (WHSV) was maintained at around 56,600 mg/g h. Prior to the activity test, samples were oxidized in an air flow at 200 °C for 120 min and then purged with an inlet feed gas mixture for 20 min. The reactor was placed into a furnace (MTI Corporation, GSL-1100X), and the catalyst temperature was monitored by a K-type thermocouple (OMEGA, HH802U) placed in the middle of the catalyst bed. The furnace temperature was programmed from 30 to 450 °C. A duration of 80 min was held at each temperature; the ramping rate was 10 °C/min. The effluent gases were analyzed by gas chromatography (SRI Instruments) with a flame ionization detector (FID) and a thermal conductivity detector (TCD). The gas lines were heated to prevent water condensation.

The catalytic activity of the samples was evaluated using the temperature required to achieve 50% methane conversion (T_{50}). The methane conversion ($\%X_{CH_4}$) is defined as

$$\%X_{CH_4} = \frac{C_{CH_4,inlet} - C_{CH_4,outlet}}{C_{CH_4,inlet}} \times 100\% \quad (5)$$

where $C_{CH_4,inlet}$ and $C_{CH_4,outet}$ are the inlet and outlet CH_4 concentrations in the feed stream, respectively. The reaction rates of methane conversion are calculated by eq 6,

$$r_{CH_4} = \frac{C_{CH_4,inlet} \times \%X_{CH_4} \times V_{gas}}{m_{Pd}} \quad [mol\ s^{-1}\ g_{Pd}^{-1}] \quad (6)$$

where V_{gas} and $C_{CH_4,inlet}$ are the flow rate and the average methane concentration at the inlet, respectively. Finally, the turnover frequency (r_{TOF}) is calculated by eq 7,

$$r_{TOF} = \frac{r_{CH_4} \times M_{Pd}}{D_{Pd}} \quad [s^{-1}] \quad (7)$$

where r_{CH_4}, M_{Pd}, and D_{Pd} are the methane conversion rate, the atomic weight of Pd, and the Pd dispersion, respectively.

3. RESULTS AND DISCUSSION

3.1. Structure and Morphology of Catalysts. The XRD patterns of samples, including the commercial ZrO_2 and CeO_2 reference samples, are provided in Figure 2a–c. The diffraction peaks at 28.5°, 33.0°, 47.4°, 56.3°, 58.9°, and 69.4° can be attributed to the (111), (200), (220), (311), (222), and (400) planes of the CeO_2 cubic fluorite structure, respectively.[27,31] The diffraction peaks at 30.3°, 34.6°, 35.4°, 50.3°, 50.8°, 59.5°, 60.3°, and 62.9° can be assigned to the (101), (002), (110), (112), (200), (103), (211), and (202) planes of the ZrO_2 tetragonal phase, respectively.[32] The XRD data of Pd (JCPDS Card No. 46-1043) and PdO (JCPDS Card No. 43-1024) are plotted at the bottom of each figure. Pd diffraction peaks cannot be observed due to the low Pd amount, which is common for Pd/CeO_2 catalysts.[33,34] $Pd/Ce_{0.67}Zr_{0.33}O_2$ samples show only a cubic fluorite structure (Figure 2a), with crystallite sizes ranging from 6 to 9 nm (Table 1), indicating the formation of a solid solution. When the Zr concentration is higher than the host concentration (Ce), $Pd/Ce_{0.33}Zr_{0.67}O_2$ samples do not preserve the cubic fluorite structure, as shown in Figure 2c, which is consistent with the literature.[35] At equimolar Zr and Ce compositions, FSP synthesis conditions can determine the formation of a solid solution structure. As shown in Figure 2b, $Pd/Ce_{0.5}Zr_{0.5}O_2$ samples synthesized at L2O5 and L2O4 have the cubic fluorite structure without phase separation, while $Pd/Ce_{0.5}Zr_{0.5}O_2$ samples synthesized at L3O5 indicate an additional peak at 30.1° which could be induced by the tetragonal ZrO_2 (101) plane. L3O5 has an equivalence ratio of 1.2, which leads to an oxygen-deficient environment that may not favor a solid solution formation. When $Pd/Ce_{0.5}Zr_{0.5}O_2$ and $Pd/Ce_{0.67}Zr_{0.33}O_2$ samples are compared, the diffraction peaks gradually shift to higher 2θ values with increasing Zr percentage. As shown in Figure 2d, the lattice constant (a) decreases linearly with increasing Zr percentage, in agreement with Vegard's law.[31] This is because the radius of Zr^{4+} ions (0.84 Å) is smaller than that of Ce^{4+}

https://doi.org/10.1021/acs.energyfuels.4c01888
Energy Fuels 2024, 38, 15571−15586

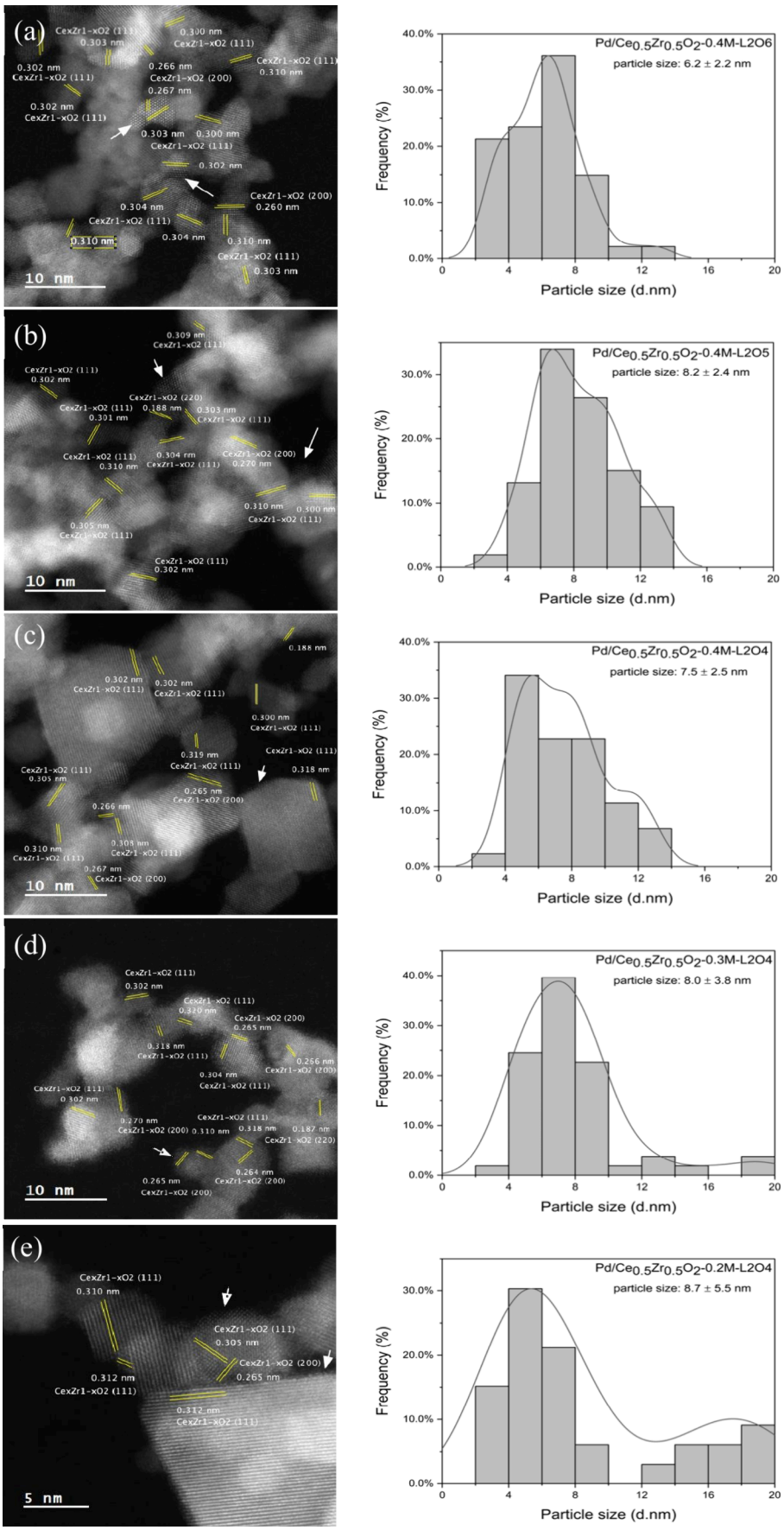

Figure 3. HAADF-STEM image and particle size distribution of (a) Pd/$Ce_{0.5}Zr_{0.5}$-0.4M-L2O6, (b) Pd/$Ce_{0.5}Zr_{0.5}$-0.4M-L2O5, (c) Pd/$Ce_{0.5}Zr_{0.5}$-0.4M-L2O4, (d) Pd/$Ce_{0.5}Zr_{0.5}$-0.3M-L2O4, and (e) Pd/$Ce_{0.5}Zr_{0.5}$-0.2M-L2O4.

https://doi.org/10.1021/acs.energyfuels.4c01888
Energy Fuels 2024, 38, 15571−15586

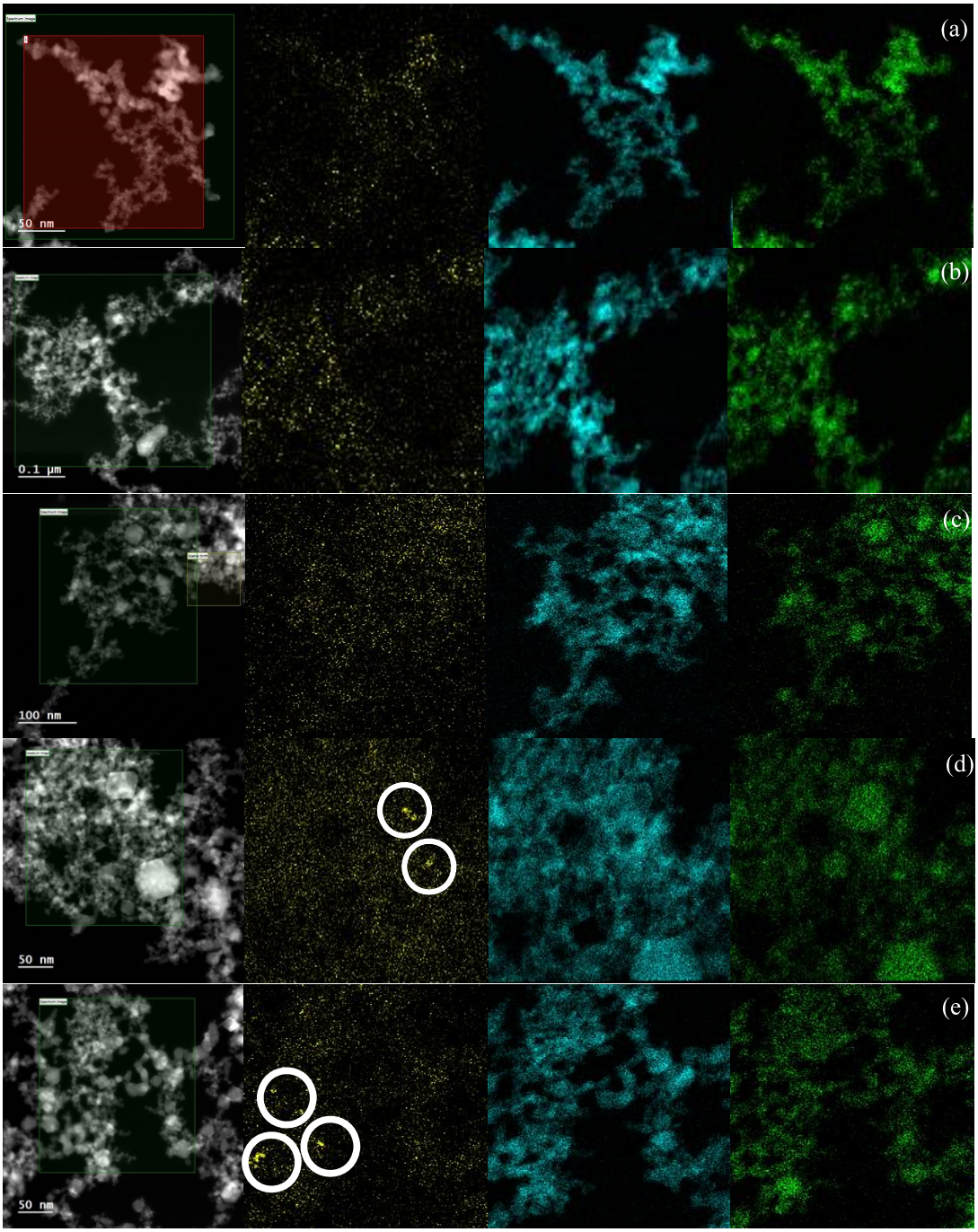

Figure 4. STEM bright-field images and STEM-EDS elemental mappings of (a) Pd/$Ce_{0.5}Zr_{0.5}$-0.4M-L2O6, (b) Pd/$Ce_{0.5}Zr_{0.5}$-0.4M-L2O5, (c) Pd/$Ce_{0.5}Zr_{0.5}$-0.4M-L2O4, (d) Pd/$Ce_{0.5}Zr_{0.5}$-0.3M-L2O4, and (e) Pd/$Ce_{0.5}Zr_{0.5}$-0.2M-L2O4. Pd, Ce, and Zr are shown as yellow, blue, and green, respectively.

ions (0.97 Å) and the unit cell gradually shrinks when more Zr^{4+} cations are incorporated into the lattice structure.[10,36,37]

The solid solution samples are down-selected to investigate the impact of precursor molarity (at the fixed liquid and oxygen flow rates, i.e., Pd/$Ce_{0.5}Zr_{0.5}O_2$-L2O4) and liquid and oxygen flow rates (at the fixed molarity, i.e., Pd/$Ce_{0.67}Zr_{0.33}O_2$-0.4M and Pd/$Ce_{0.5}Zr_{0.5}O_2$-0.4M) on the catalyst's structure and catalytic performance. Because the Pd/$Ce_{0.5}Zr_{0.5}O_2$-0.4M-L3O5 sample is not a perfect solid solution, an additional synthesis condition (L2O6) is considered. This decision was made based on our machine learning model,[38] which suggested that the perfect solid solution could be produced in Pd/$Ce_{0.5}Zr_{0.5}O_2$-0.4M-L2O6.

The specific surface areas (S_{BET}) and equivalent BET particle size (d_{BET}) are presented in Table 1. Pd/$Ce_{0.5}Zr_{0.5}O_2$-0.2M-L2O4 and Pd/$Ce_{0.5}Zr_{0.5}O_2$-0.3M-L2O4 exhibit smaller S_{BET} compared to Pd/$Ce_{0.5}Zr_{0.5}O_2$-0.4M-L2O4, which is consistent with the crystallite size calculated by XRD and particle size measured from STEM images (Table 1). This trend is attributed to the aggregation of the primary particles for catalysts synthesized at higher flame temperature environments. The relatively large S_{BET} and small particle size of Pd/$Ce_{0.5}Zr_{0.5}O_2$-0.4M-L2O6 are due to the high oxygen flow rate

https://doi.org/10.1021/acs.energyfuels.4c01888
Energy Fuels 2024, 38, 15571−15586

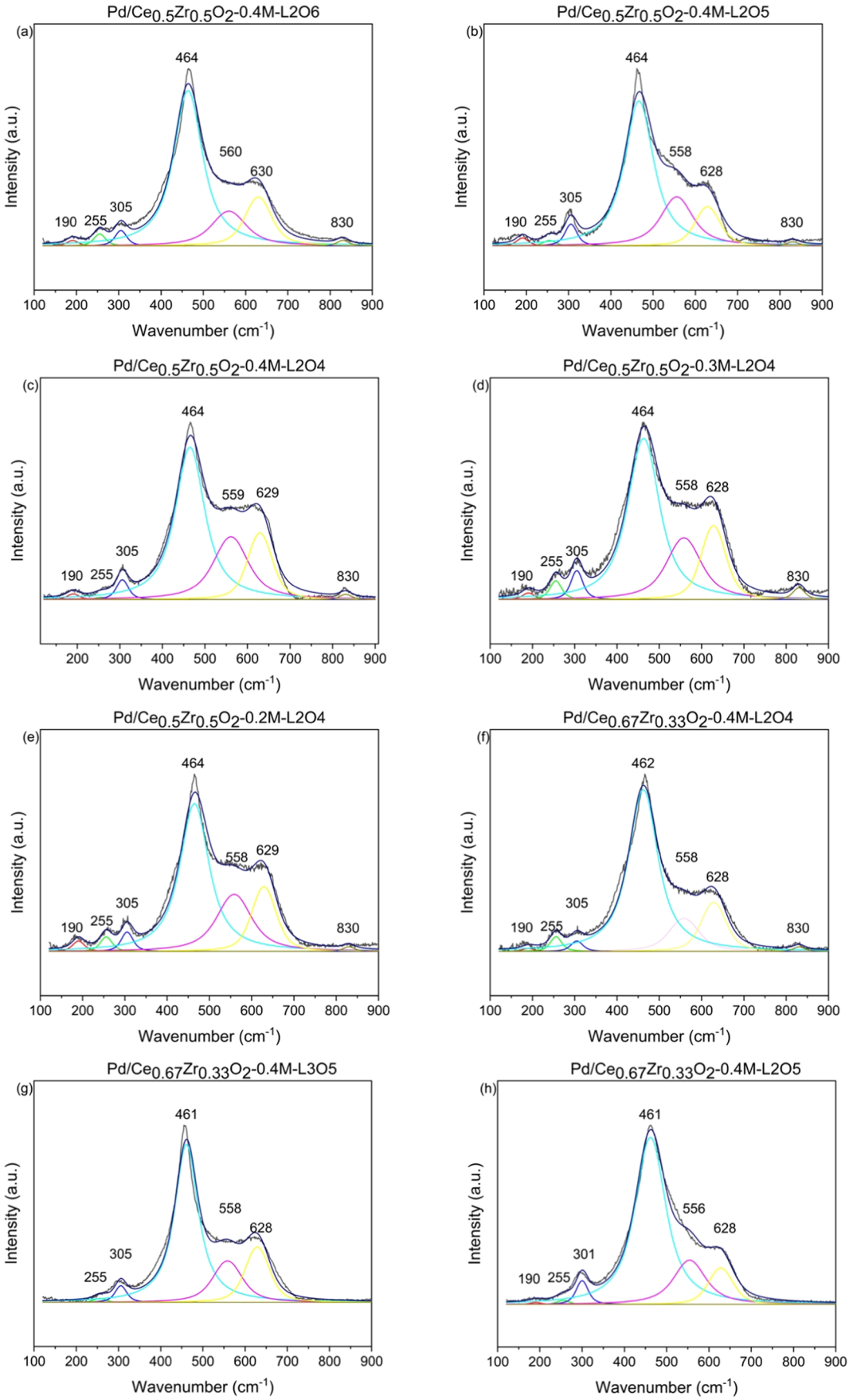

Figure 5. Raman spectra of (a) Pd/$Ce_{0.5}Zr_{0.5}O_2$-0.4M-L2O6, (b) Pd/$Ce_{0.5}Zr_{0.5}O_2$-0.4M-L2O5, (c) Pd/$Ce_{0.5}Zr_{0.5}O_2$-0.4M-L2O4, (d) Pd/$Ce_{0.5}Zr_{0.5}O_2$-0.3M-L2O4, (e) Pd/$Ce_{0.5}Zr_{0.5}O_2$-0.2M-L2O4, (f) Pd/$Ce_{0.67}Zr_{0.33}O_2$-0.4M-L2O4, (g) Pd/$Ce_{0.67}Zr_{0.33}O_2$-0.4M-L3O5, and (h) Pd/$Ce_{0.67}Zr_{0.33}O_2$-0.4M-L2O5 samples.

https://doi.org/10.1021/acs.energyfuels.4c01888
Energy Fuels 2024, 38, 15571−15586

used in synthesis. A high oxygen flow rate provides a fast-quenching rate, reducing the residence time of particles in the flame region, and thus confines the particle size to remain small.

The HAADF-STEM images of samples and their particle size distributions are shown in Figure 3. The nanostructures shown in the HAADF-STEM images are identified as $Ce_xZr_{1-x}O_2$ crystallites with the lattice fringes of 3.04, 2.67, and 1.87 Å, corresponding to the (111), (200), and (220) planes of cubic $Ce_xZr_{1-x}O_2$, respectively. The average particle sizes of $Ce_xZr_{1-x}O_2$ nanoparticles are calculated for each sample, which are similar to their crystallite sizes, as shown in Table 1. The particle size distributions in Figure 3a−c indicate a single distribution averaging around 6−8 nm, whereas larger particles around 20 nm can be observed in Figure 3d,e. The heterogeneous particle size distribution observed at 0.2 and 0.3 M can be attributed to the higher combustion enthalpy density, which can increase flame temperature and accelerate particle size growth.

Detailed analysis of the HAADF-STEM images indicates that Pd is mostly well-dispersed over the support, and no segregated Pd entities are observed. Despite the challenges of extracting any definitive conclusion from the images, the dangling atoms located at the outermost surface of the (200) plane and the rows located at the (111) surface (marked by white arrows in Figure 3) might indicate the presence of highly dispersed atoms and a monolayer of Pd atoms or islands, respectively. As shown in Figure 4, the STEM-EDS elemental mappings of samples mostly show highly dispersed Pd species on the $Ce_{0.5}Zr_{0.5}O_2$ support. However, larger PdO NPs can be observed on Pd/$Ce_{0.5}Zr_{0.5}O_2$-0.3M-L2O4 and Pd/$Ce_{0.5}Zr_{0.5}O_2$-0.2M-L2O4 (marked by white circles in Figure 4d,e), which is consistent with the larger particle sizes and larger equivalent BET particle size observed on these samples. Additionally, the STEM-EDS elemental spectra of these five samples (shown in Figure 4) are provided in Figure S1. Figure S1f depicts the K-shell emission lines of C and Cu of the carbon−copper grid used in the experiment. The emissions lines of O, Co, Fe, and Si are attributed to the background. When comparing Figure S1a−e to Figure S1f, no impurities were detected on the catalysts.

3.2. Oxygen Vacancy Formation. The formation of OVs can facilitate electron transfer at the metal and support interface[13] and can be characterized using Raman spectroscopy.[39] As shown in Figure 5, the vibrational band at 464 cm^{-1} is assigned to the F_{2g} band, which is induced by the short-range order and chemical bonds-breathing mode of the Ce−O interaction in the fluorite structure.[40,41] The band at 560 cm^{-1} is assigned to defect structures that include O^{2-} vacancies in the CeO_2 lattice,[31,42] while the band at 630 cm^{-1} is attributed to ZrO_8-type defects.[22,42−45] The band at 255 cm^{-1} can be assigned to the second-order transverse acoustic (2TA)[46] or the t′-phase of ZrO_2.[31,45] The 305 cm^{-1} band shows a small displacement of oxygen atoms on the axis, which implies the presence of t″-phase ZrO_2.[43] Both t′- and t″-phases of ZrO_2 can only exist in the $Ce_xZr_{1-x}O_2$ solid solution system.[32] Typically, the tetragonal ZrO_2 phase shows vibrational bands at 149, 224, 292, 324, 407, and 456 cm^{-1}.[27] These bands are not observed in our samples, indicating the formation of a solid solution, which is consistent with the XRD analyses.

The F_{2g} band, a key indicator of oxygen sublattice disorder and nonstoichiometry, offers valuable insights into the local environment of Ce^{4+} ions. The Raman spectra of 0.8 wt% Pd/CeO_2-0.4M-L2O4 synthesized using FSP are shown in Figure S2, in which a narrow F2g band at 457 cm^{-1} is observed. In comparison to the Raman spectra of pure CeO_2, the broadening and shift of the F_{2g} band from 457 to 464 cm^{-1} indicate a degraded symmetry of the cubic fluorite structure. This is a result of the incorporation of Zr^{4+} cations into the CeO_2 lattice, suggesting a higher presence of surface oxygen deficiencies in the $Ce_xZr_{1-x}O_2$ solid solution than in pure CeO_2.[47] The Raman spectroscopy of pure CeO_2 in Figure S2 revealed an OV peak in the 615−625 cm^{-1} range, indicating an OV% of 11.7%. By incorporating dopants such as Zr or Pd into the CeO_2 lattice, the OV% can be enhanced up to 27.2%. This enhancement in the OV concentration, as reflected by the Raman spectra, is consistent with previous literature findings.[22,43] The introduction of dopants into the CeO_2 lattice induces a distortion in the crystal structure, promoting the formation of OVs.[31] This enhancement of OVs in the $Ce_xZr_{1-x}O_2$ solid solution increases both the reducibility of the bulk and the oxygen mobility from bulk to the surface, thereby providing more surface oxygen species.[48]

The detection of the O−O stretching of peroxide species (O_2^{2-}) adsorbed on surface defect sites at 830 cm^{-1} [45,49,50] further confirms the existence of surface OVs on $Ce_xZr_{1-x}O_2$ supports. The absence of peroxide species in both Pd/$Ce_{0.67}Zr_{0.33}O_2$-0.4M-L3O5 and Pd/$Ce_{0.67}Zr_{0.33}O_2$-0.4M-L2O5 samples suggests a lower amount of surface OVs and a weaker interaction between Pd and the $Ce_xZr_{1-x}O_2$ support.

The band observed at 190 cm^{-1} on all samples (except Pd/$Ce_{0.67}Zr_{0.33}$-0.4M-L3O5) can be assigned to the A_1 mode of the highly dispersed Pd^{2+} structures stabilized in a PdO_4 square-planar coordination environment in the fluorite structure.[47,49,50] It is important to note that the B_1 mode of the PdO_4 square-planar structure, typically located around 652 cm^{-1}, may not be detected due to the relatively large OV band (630 cm^{-1}). The absence of the 190 cm^{-1} band on Pd/$Ce_{0.67}Zr_{0.33}$-0.4M-L3O5 could be associated with the reducing synthesis environment (ER = 1.2), which may not favor the substitution of Pd atoms into the $Ce_xZr_{1-x}O_2$ lattice. This observation aligns well with the DRIFTS results (Section 3.4).

As shown in Table 1, the OV% of samples follows the order of Pd/$Ce_{0.5}Zr_{0.5}O_2$-0.4M-L2O4 ≈ Pd/$Ce_{0.5}Zr_{0.5}O_2$-0.3M-L2O4 ≈ Pd/$Ce_{0.5}Zr_{0.5}O_2$-0.2M-L2O4 > Pd/$Ce_{0.5}Zr_{0.5}O_2$-0.4M-L2O5 > Pd/$Ce_{0.5}Zr_{0.5}O_2$-0.4M-L2O6 > Pd/$Ce_{0.67}Zr_{0.33}O_2$-0.4M-L2O4 > Pd/$Ce_{0.67}Zr_{0.33}O_2$-0.4M-L3O5 > Pd/$Ce_{0.67}Zr_{0.33}O_2$-0.4M-L2O5. The OV%s of all Pd/$Ce_{0.5}Zr_{0.5}O_2$ samples are above 23%, higher than those of Pd/$Ce_{0.67}Zr_{0.33}O_2$ samples. This is because OV% is correlated with the Zr ion amount incorporated into the CeO_2 lattice and Pd/$Ce_{0.5}Zr_{0.5}O_2$ has low OV formation energy.[51] The ERs for Pd/$Ce_{0.5}Zr_{0.5}O_2$-0.4M samples produced at L2O4, L2O5, and L2O6 are 1.05, 0.84, and 0.70, respectively (Table 1), indicating that decreasing the oxygen flow rate induces more OV% in Pd/$Ce_{0.5}Zr_{0.5}O_2$-0.4M samples. Similarly, an increase in the liquid flow rate can generate more OV in the samples. Pd/$Ce_{0.67}Zr_{0.33}O_2$-0.4M-L3O5 has a higher ER (1.14) compared to the ER (0.76) of Pd/$Ce_{0.67}Zr_{0.33}O_2$-0.4M-L2O5, inducing more oxygen defects. However, Pd/$Ce_{0.67}Zr_{0.33}O_2$-0.4M-L3O5 and Pd/$Ce_{0.67}Zr_{0.33}O_2$-0.4M-L2O5 have the lowest OV% among all samples, which might be associated with the absence of peroxide species at 830 cm^{-1}, as discussed in Section 3.3. Lastly, the Pd/$Ce_{0.5}Zr_{0.5}O_2$-0.4M-L2O4, Pd/$Ce_{0.5}Zr_{0.5}O_2$-0.3M-L2O4, and Pd/$Ce_{0.5}Zr_{0.5}O_2$-0.2M-L2O4 samples are synthesized at different precursor molarities but

https://doi.org/10.1021/acs.energyfuels.4c01888
Energy Fuels 2024, 38, 15571−15586

have similar ERs (around 1.0). Therefore, they show similar OV%s, suggesting that precursor molarity does not affect the OV formation.

To verify the impact of different oxygen flow rates on the Ce^{3+} ratio and OV formation in the catalysts, the photoelectron spectra of Ce 3d, O 1s, Pd 3d, and Zr 3p core levels for Pd/$Ce_{0.5}Zr_{0.5}O_2$-0.4M-L2O4, Pd/$Ce_{0.5}Zr_{0.5}O_2$-0.4M-L2O5, and Pd/$Ce_{0.5}Zr_{0.5}O_2$-0.4M-L2O6 are collected, as shown in Figure 6a–c. The binding energies of these samples after the peak fitting has been performed are listed in Table S1. The core-level spectra of Ce 3d reveal the presence of Ce^{3+} and Ce^{4+}, as shown in Figure 6a and Table S1a. Each core level ($3d_{5/2}$ and $3d_{3/2}$) exhibits two satellite peaks associated with Ce^{3+}.[52,53] Specifically, the $3d_{5/2}$ satellite peaks at u_0 = 881 eV and u′ = 884 eV, and the $3d_{3/2}$ satellite peaks at v_0 = 900 eV and v′ = 903 eV, indicate the existence of OVs in the $Ce_{0.5}Zr_{0.5}O_2$ support. Additional satellite peaks (u = 882 eV, u″ = 889 eV, and u‴ = 898 eV for $3d_{5/2}$; and v = 901 eV, v″ = 908 eV, and v‴ = 916 eV for $3d_{3/2}$) are attributed to Ce^{4+}, resulting from interactions with the Ce 4f valence electrons after the 3d core electron is emitted.[52,53] The ratio of Ce^{3+} to Ce^{4+} (Table 1) is determined by the ratio of the sum of the areas of the peaks corresponding to Ce^{3+} (u_0, u′, v_0, v′) to the sum of the areas of the peaks corresponding to both Ce^{3+} and Ce^{4+} (u, u″, u‴, v, v″, v‴). The sample with a higher Ce^{3+} ratio in XPS demonstrates a greater concentration of OVs, as confirmed by Raman spectroscopy. This correlation indicates that the increase in Ce^{3+} ions is associated with the formation of OVs in the CeO_2 lattice.

Figure 6b shows the O 1s core-level signal of the fresh Pd/$Ce_{0.5}Zr_{0.5}O_2$ samples. As shown in Table S1b, three oxygen species are present on the surface of the Pd/$Ce_{0.5}Zr_{0.5}O_2$ catalysts.[54] The first species, with a binding energy of 529 eV, is characteristic of lattice oxygen (O_α) associated with $Ce_{0.5}Zr_{0.5}O_2$ support. The species at 531 eV can be assigned to defective oxygen sites (O_β), which are considered to be more reactive than lattice oxygen due to higher mobility. The species (O_γ) at 532–533 eV is due to hydroxyl groups or adsorbed water. The O_β concentration can be associated with the activity; its relative concentration ratios are shown in Table 1. Notably, Pd/$Ce_{0.5}Zr_{0.5}O_2$-0.4M-L2O4 exhibited the highest relative concentration of O_β, matching well with the OV% ranking calculated by Raman spectroscopy. This further supports the result that OV formation increases with the decrease in oxygen flow rate.

3.3. Reduction Profile and Metal–Support Interaction. The TPR profiles of solid solution samples consist of multiple hydrogen consumption peaks, as shown in Figure 7. The α (70–120 °C), β (120–180 °C), γ (180–250 °C), δ (250–450 °C), and θ (>650 °C) peaks are attributed to the reduction of finely dispersed PdO species, Pd^{2+} incorporated into $Ce_xZr_{1-x}O_2$, lattice oxygen derived from nonstoichiometric $Ce_xZr_{1-x}O_{2-y}$, surface oxygen of bulk $Ce_xZr_{1-x}O_2$, and lattice oxygen of bulk $Ce_xZr_{1-x}O_2$, respectively.[27,47−50,55−57] The TPR profiles of pure CeO_2 or ZrO_2 are documented in the literature.[58,59] In the TPR profile of pure CeO_2,[58] the peaks at 550 and 875 °C correspond to the reduction of surface Ce^{4+} and bulk Ce^{4+} species to Ce^{3+}, respectively. Unlike CeO_2, ZrO_2 is highly stable, and its TPR profile shows minimal to no reduction peaks, with a typically flat profile, indicating minimal reduction up to 900 °C.[60] Compared to the TPR profile of Pd/CeO_2,[49] the α, γ, and δ peaks shift to lower temperatures due to the weak metal–support interaction between Pd and the

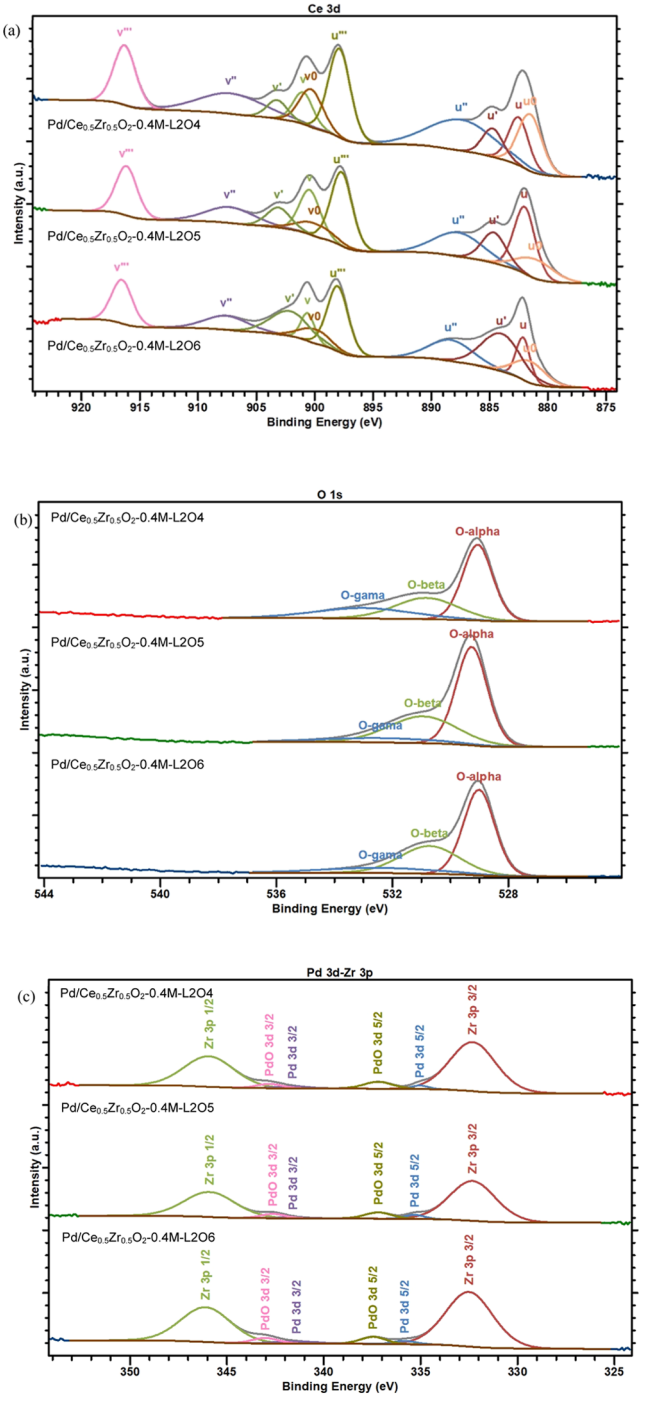

Figure 6. XPS spectra of the (a) Ce 3d core level, (b) O 1s core level, and (c) Pd 3d and Zr 3p core level of Pd/$Ce_{0.5}Zr_{0.5}O_2$-0.4M-L2O4, Pd/$Ce_{0.5}Zr_{0.5}O_2$-0.4M-L2O5, and Pd/$Ce_{0.5}Zr_{0.5}O_2$-0.4M-L2O6 samples. u and v refer to the $3d_{5/2}$ and $3d_{3/2}$ spin–orbit components, respectively.

$Ce_xZr_{1-x}O_2$ support, which facilitates electron transfer, increasing the reoxidation rate of Pd^0 to Pd^{2+}.[10−12,49] A double-peak feature in the α region is only shown for Pd/$Ce_{0.5}Zr_{0.5}O_2$-0.2M-L2O4, which could be related to the two-step reduction of PdO species to Pd_2O and Pd.[56] The reduction temperature of the α peak follows the order of Pd/$Ce_{0.5}Zr_{0.5}O_2$-0.4M-L2O4 ≈ Pd/$Ce_{0.5}Zr_{0.5}O_2$-0.3M-L2O4 ≈ Pd/$Ce_{0.5}Zr_{0.5}O_2$-0.2M-L2O4 ≈ Pd/$Ce_{0.5}Zr_{0.5}O_2$-0.4M-L2O5 < Pd/$Ce_{0.5}Zr_{0.5}O_2$-0.4M-L2O6 < Pd/$Ce_{0.67}Zr_{0.33}O_2$-0.4M-

https://doi.org/10.1021/acs.energyfuels.4c01888
Energy Fuels 2024, 38, 15571−15586

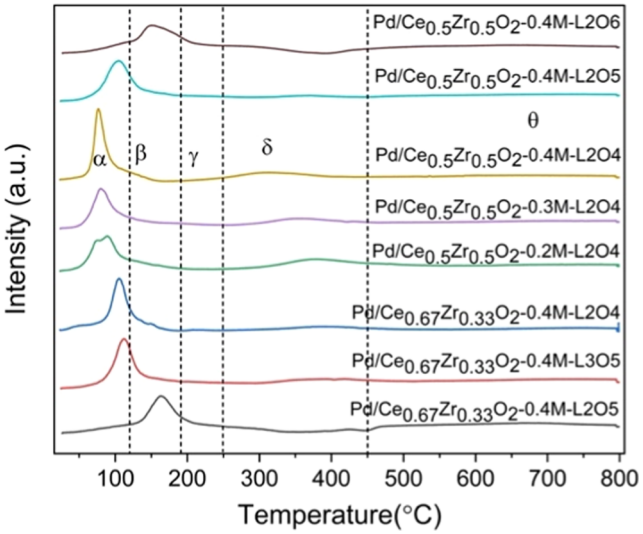

Figure 7. TPR of $Pd/Ce_{0.5}Zr_{0.5}O_2$ and $Pd/Ce_{0.66}Zr_{0.33}O_2$ solid solution samples synthesized at different precursor molarity, liquid, and oxygen flow rates.

L2O4 < $Pd/Ce_{0.67}Zr_{0.33}O_2$-0.4M-L3O5 < $Pd/Ce_{0.67}Zr_{0.33}O_2$-0.4M-L2O5. A lower reduction temperature for finely dispersed PdO species indicates a weaker metal−support interaction[56] and better oxygen mobility.[61,62] This order follows the OV% ranking, indicating that the higher OV% in the $Ce_xZr_{1-x}O_2$ solid solution support can induce a weaker metal−support interaction and facilitate the formation of finely dispersed PdO species.

The $Pd/Ce_{0.67}Zr_{0.33}O_2$-0.4M-L3O5 and $Pd/Ce_{0.67}Zr_{0.33}O_2$-0.4M-L2O5 samples have the lowest OV%, hence the strongest metal−support interaction. The peroxide species (O_2^{2-}) adsorbed on the two-electron defect sites on the support surface[50] can act as intermediates during the reoxidation of the reduced support,[45] facilitating the electron transfer from Ce^{3+} to Ce^{4+}. Considering that electron transfer is not favored on a sample with strong metal−support interaction, the peroxide species at 830 cm^{-1} would not be observed on a sample with low OV%.

XRD patterns for the spent samples following TPR experiments indicate the formation of a cubic fluorite structure, as shown in Figure S3. Figure S3 indicates that none of the samples showed distinct t-phase ZrO_2 after TPR, indicating the excellent thermal stability of the support.

The $Pd/Ce_{0.5}Zr_{0.5}O_2$-0.4M-L2O4, $Pd/Ce_{0.5}Zr_{0.5}O_2$-0.3M-L2O4, $Pd/Ce_{0.5}Zr_{0.5}O_2$-0.2M-L2O4, $Pd/Ce_{0.5}Zr_{0.5}O_2$-0.4M-L2O5, and $Pd/Ce_{0.67}Zr_{0.33}O_2$-0.4M-L2O4 samples exhibit a small β peak at the tail of the α peak. Pd^{2+} incorporated into the $Ce_xZr_{1-x}O_2$ support is more difficult to reduce than finely dispersed PdO species, consistent with the literature.[47,50,55] However, in the case of $Pd/Ce_{0.5}Zr_{0.5}O_2$-0.4M-L2O6 and $Pd/Ce_{0.67}Zr_{0.33}O_2$-0.4M-L2O5, the broad β peak implies that more Pd is incorporated into the solid solution support. The 190 cm^{-1} band in the Raman spectra agrees well with the incorporated Pd^{2+} species in the TPR. The $Pd/Ce_{0.67}Zr_{0.33}O_2$-0.4M-L3O5 sample does not have incorporated Pd^{2+} species, as shown by the absence of a β reduction peak and a 190 cm^{-1} band.

The amount of reducible oxygen extracted from a catalyst can be determined by the H_2 consumption of each reduction peak. The theoretical H_2 consumption for reducing all PdO species is 3.76 μmol g^{-1} based on the total Pd amount. However, the total H_2 consumption of all catalysts (Table 1) is much higher than this value, indicating the back spillover of oxygen from the $Ce_xZr_{1-x}O_2$ support to the Pd.[49,57] The $Pd/Ce_{0.5}Zr_{0.5}O_2$ samples exhibit a larger total H_2 consumption than the $Pd/Ce_{0.67}Zr_{0.33}O_2$ ones, which is consistent with the OV% amount calculated from their Raman spectra. Although the total H_2 consumptions for $Pd/Ce_{0.5}Zr_{0.5}O_2$-0.2M-L2O4 (679.8 μmol g^{-1}) and $Pd/Ce_{0.5}Zr_{0.5}O_2$-0.3M-L2O4 (674.9 μmol g^{-1}) are lower than that for $Pd/Ce_{0.5}Zr_{0.5}O_2$-0.4M-L2O4 (756.2 μmol g^{-1}), all three catalysts have comparable OV%s since their ERs are the same (Table 1). This suggests that Pd dispersion plays a crucial role in H_2 consumption since it facilitates H_2 spillover.[63] As shown in STEM-EDS mapping (Figure 4), higher precursor molarity has a lower flame temperature, leading to a high Pd dispersion. When comparing different liquid and oxygen flow rates for $Pd/Ce_{0.5}Zr_{0.5}O_2$-0.4M samples, L2O6 exhibits a higher total H_2 consumption than L2O5 and L2O4. Since these samples have a similar Pd dispersion, the higher H_2 reduction ability of L2O6 may be related to the incorporated Pd^{2+} species, as they can facilitate oxygen transfer. This also suggests that a higher oxygen flow rate and a lower ER can favor the formation of incorporated Pd^{2+} species.

Pd dispersion of solid solution samples ranges from 18% to 26%, as shown in Table 1. Samples synthesized at 0.4 M show similar Pd dispersion, suggesting that the Ce:Zr element ratio and liquid and oxygen flow rates do not affect Pd dispersion. The comparison between samples synthesized at 0.2, 0.3, and 0.4 M suggests that the higher flame temperature can promote the growth of nanoparticles and decrease dispersion. The 0.2 M sample has a much lower dispersion (18.7%) than the 0.4 M sample, suggesting the formation of aggregated Pd species, which agrees well with the STEM-EDS elemental mappings of 0.2 and 0.3 M samples (Figure 4d,e). It is important to note that Pd dispersions on solid solution catalysts synthesized in this work are in the range of those synthesized using solvent-thermal, coprecipitation, sol−gel, solution-combustion, and wet impregnation synthesis processes.[15−17,64]

3.4. Surface Speciation of Pd Species. Pd 3d core-level spectra of $Pd/Ce_{0.5}Zr_{0.5}O_2$-0.4M-L2O4, $Pd/Ce_{0.5}Zr_{0.5}O_2$-0.4M-L2O5, and $Pd/Ce_{0.5}Zr_{0.5}O_2$-0.4M-L2O6 samples in Figure 6c exhibit two Pd $3d_{5/2}$ peaks, at 335 and 337 eV for Pd^0 and Pd^{2+}, respectively. As shown in Table S1c, the binding energy of Pd^0 is consistent with the previously reported values for Pd foil at 334.9 eV. However, the binding energy of Pd^{2+} is higher than the reported value of PdO (336.8 eV), suggesting that the PdO NPs are highly dispersed, consistent with the DRIFTS and STEM data.[65] Additionally, Zr 3p core-level photoelectron spectroscopy shows a single peak at 332.9 eV for Zr $3p_{3/2}$, corresponding to ZrO_2.[66,67] The ratio of Pd^{2+} was calculated based on the areas of Pd $3d_{5/2}$ core-level peaks for Pd^{2+} and Pd^0. As shown in Table 1, $Pd/Ce_{0.5}Zr_{0.5}O_2$-0.4M-L2O6 has the highest ratio of Pd^{2+} among the three samples, consistent with its highest total H_2 consumption in the TPR results.

In X-ray photoelectron spectroscopy (XPS), the characterization of Pd/CeO_2 structures can differentiate between large and dispersed PdO NPs. However, it fails to differentiate atomically dispersed PdO structures, as all dispersed PdO species show a Pd^{2+} binding energy at 337 eV.[34] To determine Pd speciation on solid solution samples, in situ CO adsorption DRIFTS experiments were carried out.[34,68] As shown in Figure 8, the Pd-CO adsorption bands are separated into four regions.

https://doi.org/10.1021/acs.energyfuels.4c01888
Energy Fuels 2024, 38, 15571−15586

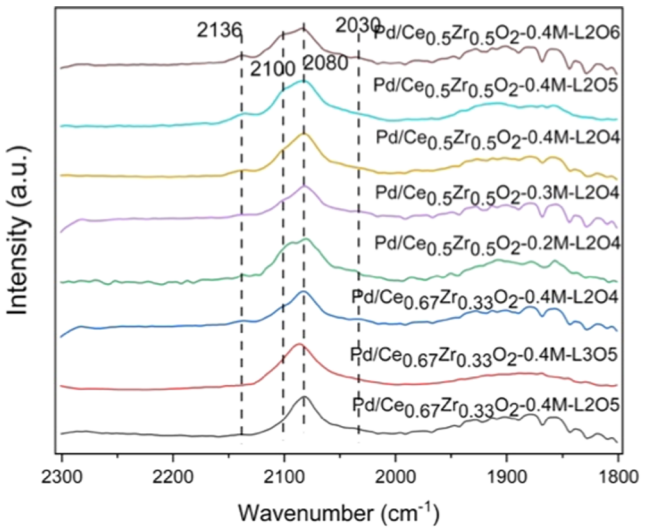

Figure 8. Room temperature CO adsorption DRIFTS of Pd/$Ce_{0.5}Zr_{0.5}O_2$-0.4M-L2O6, Pd/$Ce_{0.5}Zr_{0.5}$-0.4M-L2O5, Pd/$Ce_{0.5}Zr_{0.5}O_2$-0.4M-L2O4, Pd/$Ce_{0.5}Zr_{0.5}O_2$-0.3M-L2O4, Pd/$Ce_{0.5}Zr_{0.5}O_2$-0.2M-L2O4, Pd/$Ce_{0.67}Zr_{0.33}O_2$-0.4M-L2O4, Pd/$Ce_{0.67}Zr_{0.33}O_2$-0.4M-L3O5, and Pd/$Ce_{0.67}Zr_{0.33}O_2$-0.4M-L2O5 after 10 min CO exposure.

In Figure S4, peak fittings for each DRIFT spectra shown in Figure 8 are displayed to clearly depict each peak. The black curve represents the raw data, while the purple curve shows the fitted composite peak. The light blue, dark blue, green, and red curves are centered at 2070, 2095, 2082, and 2136 cm^{-1}, respectively. The bands at 2082 and 2095 cm^{-1} represent linear CO adsorption at the edge and facet of Pd^0 NPs, respectively.[43,69,70] The spectral region from 2000 to 2050 cm^{-1} is associated with Pd^0 clusters covered by O atoms.[47,71,72] The wide peak in the range of 1850 to 1950 cm^{-1} is attributed to the two- and three-fold adsorption sites on Pd^0.[43,49,69,70] Pd^+ species are generally observed at 2117 cm^{-1},[49] but they are not clearly observed in our samples, possibly because of overlapping bands. The vibrational bands of Pd^{2+} structures formed over the CeO_2-based supports are controversial in the literature. Some works assign the vibrational bands between 2134 and 2139 cm^{-1} to highly dispersed Pd^{2+} species,[71,73,74] while others attribute the 2147 and 2139 cm^{-1} bands to highly dispersed, fully coordinated Pd^{2+} and coordination-unsaturated Pd^{2+} species, respectively.[47] In our study, we assigned the 2136 cm^{-1} band to the Pd^{2+} incorporated into $Ce_xZr_{1-x}O_2$.

All samples synthesized at the oxidizing environment in FSP, except Pd/$Ce_{0.67}Zr_{0.33}$-0.4M-L3O5, show incorporated Pd^{2+} species at 2136 cm^{-1}, which is consistent with the TPR analysis and peroxide band in the Raman spectra. Figure S5 depicts the time-resolved room-temperature CO adsorption DRIFTS of these samples, collected over a period of up to 30 min subsequent to exposure to 1000 ppm of CO. Pd/$Ce_{0.67}Zr_{0.33}O_2$-0.4M-L2O5 exhibits a small 2136 cm^{-1} band at 2 and 5 min of CO exposure, as shown in Figure S5h, but it gradually disappears after 10, 20, and 30 min of CO exposure. This indicates that the incorporated Pd^{2+} ions may not be stable in Pd/$Ce_{0.67}Zr_{0.33}O_2$-0.4M-L2O5. To investigate the stability of the CO adsorbed on Pd species, temperature ramping experiments were conducted up to 500 °C after exposing the samples to CO for 30 min, as shown in Figure S6. In Figure S6, DRIFT spectra were collected at intervals of 100 °C. With increasing temperature, the CO-Pd bonding (indicated by 2100 and 2080 cm^{-1} bands) weakens, leading to the desorption of some CO molecules from the Pd surface. Consequently, the intensity of these peaks decreased and in some cases disappeared. Upon cooling back down to room temperature, CO was able to readsorb onto the Pd NPs, restoring the original peaks between 2100 and 2080 cm^{-1}. These findings suggest that the CO-Pd interaction is reversible and the Pd adsorption sites are stable.

Both Pd/$Ce_{0.67}Zr_{0.33}O_2$-0.4M-L3O5 and Pd/$Ce_{0.67}Zr_{0.33}O_2$-0.4M-L2O5 do not have the peroxide band, which suggests that peroxide species are not directly associated with the formation of incorporated Pd^{2+} species. However, peroxide species can stabilize the incorporated Pd^{2+} species. Since the formation of incorporated Pd^{2+} species is related to the local negative charges at the surface OV, a sample possessing peroxide species allows fast electron transfer, stabilizing the local OV structure.

The impact of varying oxygen flow rates on the oxidation state of Pd is further explored through XANES analysis. Figure S7 shows the Pd K-edge XANES spectra of the Pd/$Ce_{0.5}Zr_{0.5}O_2$-0.4M-L2O4, Pd/$Ce_{0.5}Zr_{0.5}O_2$-0.4M-L2O5, and Pd/$Ce_{0.5}Zr_{0.5}O_2$-0.4M-L2O6 samples. Pd foil and PdO were characterized as references. The absorption edges of Pd foil and PdO are measured at 24 350.3 and 24 352.7 eV, respectively, which is consistent with the literature.[34,75] The

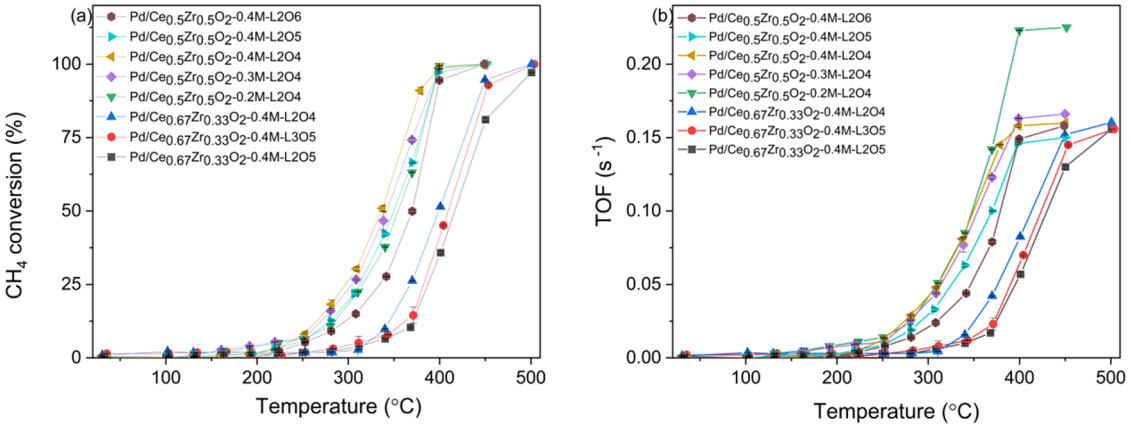

Figure 9. (a) Light-off curves and (b) TOFs of methane conversion of eight samples. The inlet gas was composed of 0.5% CH_4, 4% O_2, and balanced with N_2. The weight hourly space velocity (WHSV) was maintained at around 56,600 mg/g h.

https://doi.org/10.1021/acs.energyfuels.4c01888
Energy Fuels 2024, 38, 15571−15586

XANES spectra of all three samples are quite similar, with their absorption edges being higher than that of the Pd foil and closer to the absorption edge of PdO. This suggests that they contain both metallic Pd and Pd^{2+} states. Table 1 shows the percentages of Pd^{2+} and Pd^0 for each sample. $Pd/Ce_{0.5}Zr_{0.5}O_2$-0.4M-L2O6 has the highest Pd^{2+} ratio among these three samples, which is in line with its highest H_2 consumption, indicated by α and β peaks in the TPR results. However, the linear combination fitting cannot differentiate incorporated Pd^{2+} species from PdO NPs. Therefore, we can only summarize that a higher oxygen flow rate can produce more Pd^{2+} species on fresh samples.

3.5. Methane Oxidation Activity and Stability Test. Figure 9a,b shows the light-off curves and TOFs of $Pd/Ce_xZr_{1-x}O_2$ for methane oxidation. Figures S8 and S9 show the light-off curves and TOFs of methane conversion of samples grouped into three categories: (a) $Pd/Ce_{0.67}Zr_{0.33}O_2$ samples synthesized at 0.4 M with varying liquid and oxygen flow rates, (b) $Pd/Ce_{0.5}Zr_{0.5}O_2$ samples synthesized at 0.4 M and L2 with varying oxygen flow rate, and (c) $Pd/Ce_{0.5}Zr_{0.5}O_2$ samples synthesized at L2O4 with varying molarities. The TOFs range from 0.10 to 0.21 s^{-1}, ranking in the order of $Pd/Ce_{0.5}Zr_{0.5}O_2$-0.2M-L2O4 > $Pd/Ce_{0.5}Zr_{0.5}O_2$-0.3M-L2O4 > $Pd/Ce_{0.5}Zr_{0.5}O_2$-0.4M-L2O4 > $Pd/Ce_{0.5}Zr_{0.5}O_2$-0.4M-L2O5 > $Pd/Ce_{0.5}Zr_{0.5}O_2$-0.4M-L2O6 > $Pd/Ce_{0.67}Zr_{0.33}O_2$-0.4M-L2O4 > $Pd/Ce_{0.67}Zr_{0.33}O_2$-0.4M-L3O5 > $Pd/Ce_{0.67}Zr_{0.33}O_2$-0.4M-L2O5 at temperatures below 370 °C. Table S2 summarizes the TOFs at 400 °C reported in the literature. The TOF rankings are similar to those of OV% and reduction temperatures, falling within the range of 0 to 0.16 s^{-1}. The T_{50}'s of $Pd/Ce_xZr_{1-x}O_2$ vary between 337 and 420 °C and exhibit greater initial activity than commercial $Pd/Ce_xZr_{1-x}O_2$ three-way catalysts, which have a T_{50} of 420 °C at WHSV of 56,000 mg/g h.[76] Additionally, the $Pd/Ce_{0.5}Zr_{0.5}$-0.4M-L2O4 catalyst was exposed to 5 vol% water vapor at 700 °C for 5 h. Light-off curves are collected in the absence of water vapor, as shown in Figure S10a, revealing a shift of T_{50} to 450 °C. Figure S10b illustrates the XRD results of samples following the hydrothermal stability test, indicating the absence of phase separation.

However, the crystallite size slightly increased from 7.52 to 8.19 nm. This observation suggests that the pretreatment with water vapor adversely affects the catalytic performance, potentially due to changes in the catalyst's surface properties[77] or Pd interaction with the support.[78]

3.6. Structure−Activity Relationship. Our analysis indicates that $Pd/Ce_{0.67}Zr_{0.33}O_2$-0.4M-L2O4 is more effective than -L3O5 and -L2O5 at temperatures below 450 °C, as per Figure 9b. As previously mentioned, Figure S9 depicts the light-off curves and TOFs of methane conversion for these samples, grouped into three categories. When the oxygen flow rate is increased from -L2O4 to -L2O5, it results in a lower OV % and stronger metal−support interaction, leading to the creation of fewer peroxide species, as shown in Figure 5f,h. Furthermore, $Pd/Ce_{0.67}Zr_{0.33}O_2$-0.4M-L2O4 exhibits higher Pd dispersion than -L2O5 and -L3O5, exposing more Pd species to the reactants. When $Pd/Ce_{0.67}Zr_{0.33}O_2$-0.4M-L3O5 and -L2O5 samples have comparable OV% and Pd dispersion, Pd speciation may have an impact on methane oxidation activity. According to Table 1, only PdO NPs can be seen over $Pd/Ce_{0.67}Zr_{0.33}O_2$-0.4M-L3O5, whereas the majority of Pd are incorporated Pd^{2+} species over $Pd/Ce_{0.67}Zr_{0.33}O_2$-0.4M-L2O5. The former displays higher methane oxidation activity, indicating that PdO NPs may be more effective for methane oxidation than the incorporated Pd^{2+} species at temperatures lower than 450 °C.

When comparing equimolar compositions, $Pd/Ce_{0.5}Zr_{0.5}O_2$-0.4M-L2O4 is more active for methane oxidation than -L2O5 and -L2O6, as shown in Figure 9b and Figure S9. The T_{50} of $Pd/Ce_{0.5}Zr_{0.5}O_2$-0.4M-L2O4 is 33 °C lower, and its TOF at 340 °C is 1.8 times higher than that of its -L2O6 counterpart. It is important to note that all samples have peroxide species and similar Pd dispersion (around 25%). However, the $Pd/Ce_{0.5}Zr_{0.5}O_2$-0.4M-L2O4 and -L2O5 catalysts mainly consist of PdO NPs, whereas the -L2O6 counterpart mostly contains incorporated Pd^{2+} species. Comparing the -L2O4 and -L2O5 samples with -L2O6 suggests that catalysts with higher OV% and PdO NPs have more activity than the sample with low OV % and incorporated Pd^{2+} species.

When considering the effect of molarity on activity, it has been observed that $Pd/Ce_{0.5}Zr_{0.5}O_2$-0.2M-L2O4 exhibits similar TOFs to the 0.3 and 0.4 M counterparts but becomes more active at higher temperatures ranging from 350 to 450 °C. The matching TOFs at the low-temperature range indicate that the Pd speciation is similar, consisting of mixed PdO NPs and incorporated Pd^{2+} species. However, larger PdO NPs can be observed in STEM-EDS elemental mapping of the 0.2 M catalyst, which is consistent with its Pd dispersion. This suggests that larger PdO NPs can promote methane oxidation activity at higher temperatures (>350 °C) compared to finely dispersed PdO. A similar behavior is reported in Pd/SSZ-13 and Pd/CeO_2 catalysts, where they exhibit greater activity over PdO NPs than finely dispersed PdO NPs.[79,80] The reduced activity over finely dispersed PdO NPs was explained by the resistance in activating C−H and O_2.

Our results indicate that the incorporated Pd^{2+} and peroxide species facilitate oxygen transfer. The addition of Zr cations into the CeO_2 lattice leads to an increased OV%, which can generate peroxide species (O_2^{2-}). These peroxide species act as intermediates during reoxidation of the reduced support and assist in the electron transfer from Ce^{3+} to Ce^{4+}. As revealed by TPR analysis, the incorporated Pd^{2+} species contribute to the CH_4 oxidation activity by promoting facile reoxidation of Pd to Pd^{2+}. To provide a clear illustration of the mechanism of the methane oxidation reaction on $Pd/Ce_xZr_{1-x}O_2$ solid solution catalysts, a schematic diagram is presented in Scheme 1.

Scheme 1. Schematic of $Pd/Ce_xZr_{1-x}O_2$ Solid Solution Catalysts in the Methane Oxidation Reaction

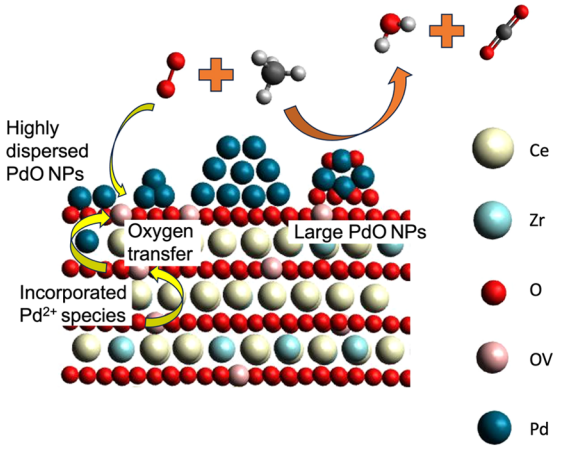

https://doi.org/10.1021/acs.energyfuels.4c01888
Energy Fuels 2024, 38, 15571−15586

Surface OVs can be replenished either by oxygen from the reactants or by lattice oxygen transferred from the support. The PdO NPs can serve as the active sites for methane activation. Compared to the highly dispersed PdO NPs, the larger PdO NPs offer a more extensive surface area for methane adsorption. Although the incorporated Pd^{2+} species may not be as active as Pd NPs, their presence enhances oxygen mobility.

4. CONCLUSIONS

Pd-deposited $Ce_xZr_{1-x}O_2$ solid solution catalysts were synthesized under various conditions using FSP to investigate the effect of synthesis parameters on catalyst morphology and methane oxidation activity. Our results indicate that FSP synthesis conditions can affect the formation of PdO nanoparticles and incorporated Pd^{2+} species in $Ce_xZr_{1-x}O_2$, allowing the control of catalysts' properties and performance in methane oxidation. Increasing the liquid feed rate or decreasing the oxygen flow rate in FSP can promote the formation of OVs. The precursor molarity did not affect the OV% of the catalyst when the ER was kept constant. The Raman spectroscopy and DRIFTS confirmed that the oxidizing synthesis environment (ER < 1) promotes the formation of incorporated Pd^{2+} species, which are less active than PdO NPs for methane oxidation. Low precursor molarity generates higher flame temperatures, resulting in low Pd dispersion and the formation of larger PdO NPs. The equimolar solid solution catalysts, i.e., $Pd/Ce_{0.5}Zr_{0.5}O_2$, show weaker metal−support interaction and OV% and facilitate the formation of peroxide species, leading to a higher methane oxidation activity. These peroxide species act as intermediates during reoxidation and electron transfer of support. By understanding the impact of the FSP synthesis conditions on catalyst structure, the T_{50} and TOF of $Pd/Ce_{0.5}Zr_{0.5}O_2$ are improved to 337 °C and 0.21 s^{-1}, respectively. The synergistic interaction of OVs and peroxide species with incorporated Pd^{2+} and PdO NPs enables low-temperature methane oxidation activity and can be controlled by FSP. Overall, these findings could facilitate the development of functional catalyst synthesis in FSP.

■ ASSOCIATED CONTENT

Supporting Information

The Supporting Information is available free of charge at https://pubs.acs.org/doi/10.1021/acs.energyfuels.4c01888.

Method to calculate error bars of OV%; comparison of OV% calculated by Raman spectroscopy and XPS; figures showing STEM-EDS elemental spectra, Raman spectra, XRD patterns, CO adsorption DRIFTS, XANES spectra, light-off curves and TOFs of CH_4 conversion, and tables of binding energy and TOF data (PDF)

■ AUTHOR INFORMATION

Corresponding Author

Erdem Sasmaz − *Department of Chemical and Biomolecular Engineering, University of California, Irvine, California 92697, United States;* orcid.org/0000-0002-4861-9406; Email: esasmaz@uci.edu

Authors

Can Wang − *Department of Chemical and Biomolecular Engineering, University of California, Irvine, California 92697, United States*

Ben Ko − *Department of Chemical and Biomolecular Engineering, University of California, Irvine, California 92697, United States*

Complete contact information is available at: https://pubs.acs.org/10.1021/acs.energyfuels.4c01888

Author Contributions

C.W. and E.S. contributed equally to this work. B.K. assisted in reaction experiments.

Funding

This work was supported by the U.S. Department of Energy Small Business Innovation Research (SBIR) Phase II grant [DE-SC0018887, 2019].

Notes

The authors declare no competing financial interest.

■ ACKNOWLEDGMENTS

We acknowledge the use of facilities and instrumentation at the UC Irvine Materials Research Institute (IMRI), which is partly supported by the National Science Foundation through the UC Irvine Materials Research Science and Engineering Center (DMR-2011967). We acknowledge Laser Spectroscopy Labs. The XAS research was performed at the Materials Research Collaborative Access Team (MRCAT). MRCAT operations are supported by the Department of Energy and the MRCAT member institutions.

■ REFERENCES

(1) Sekizawa, K.; Widjaja, H.; Maeda, S.; Ozawa, Y.; Eguchi, K. Low Temperature Oxidation of Methane over Pd/SnO_2 Catalyst. *Appl. Catal. A Gen.* **2000**, *200* (1), 211−217.

(2) Raj, A. Methane Emission Control. *Johnson Matthey Technol. Rev.* **2016**, *60* (4), 228−235.

(3) Yang, S.; Maroto-Valiente, A.; Benito-Gonzalez, M.; Rodriguez-Ramos, I.; Guerrero-Ruiz, A. Methane Combustion over Supported Palladium Catalysts I: Reactivity and Active Phase. *Appl. Catal., B* **2000**, *28* (3−4), 223−233.

(4) Worth, D. J.; Stettler, M. E. J.; Dickinson, P.; Hegarty, K.; Boies, A. M. Characterization and Evaluation of Methane Oxidation Catalysts for Dual-Fuel Diesel and Natural Gas Engines. *Emiss. Control. Sci. Technol.* **2016**, *2* (4), 204−214.

(5) Jiménez-Borja, C.; Dorado, F.; de Lucas-Consuegra, A.; García-Vargas, J. M.; Valverde, J. L. Complete Oxidation of Methane on Pd/YSZ and Pd/CeO_2/YSZ by Electrochemical Promotion. *Catal. Today* **2009**, *146* (3−4), 326−329.

(6) Cargnello, M.; Delgado Jaén, J. J.; Hernández Garrido, J. C.; Bakhmutsky, K.; Montini, T.; Calvino Gámez, J. J.; Gorte, R. J.; Fornasiero, P. Exceptional Activity for Methane Combustion over Modular Pd@CeO2 Subunits on Functionalized Al2O3. *Science* **2012**, *337* (6095), 713−717.

(7) Yang, W.; Polo-Garzon, F.; Zhou, H.; Huang, Z.; Chi, M.; Meyer, H.; Yu, X.; Li, Y.; Wu, Z. Boosting the Activity of Pd Single Atoms by Tuning Their Local Environment on Ceria for Methane Combustion. *Angew. Chem., Int. Ed.* **2023**, *62*, e202217323.

(8) Stotz, H.; Maier, L.; Boubnov, A.; Gremminger, A. T.; Grunwaldt, J. D.; Deutschmann, O. Surface Reaction Kinetics of Methane Oxidation over PdO. *J. Catal.* **2019**, *370*, 152−175.

(9) Fujimoto, K.-I.; Ribeiro, F. H.; Avalos-Borja, M.; Iglesia, E. Structure and Reactivity of PdO_x /ZrO_2 Catalysts for Methane Oxidation at Low Temperatures. *J. Catal.* **1998**, *179*, 431−442.

(10) Bozo, C.; Guilhaume, N.; Herrmann, J. M. Role of the Ceria-Zirconia Support in the Reactivity of Platinum and Palladium Catalysts for Methane Total Oxidation under Lean Conditions. *J. Catal.* **2001**, *203* (2), 393−406.

(11) Ciuparu, D.; Pfefferle, L. Contributions of Lattice Oxygen to the Overall Oxygen Balance during Methane Combustion over PdO-Based Catalysts. *Catal. Today* **2002**, *77* (3), 167−179.
(12) Liotta, L. F.; Di Carlo, G.; Pantaleo, G.; Deganello, G. Co_3O_4/CeO_2 and Co_3O_4/CeO_2-ZrO_2 Composite Catalysts for Methane Combustion: Correlation between Morphology Reduction Properties and Catalytic Activity. *Catal. Commun.* **2005**, *6* (5), 329−336.
(13) Kuznetsova, T.; Sadykov, V.; Batuev, L.; Moroz, E.; Burgina, E.; Rogov, V.; Kriventsov, V.; Kochubey, D. Modified Ceria-Zirconia Fluorite-Like Catalysts for the Combustion of Methane. *J. Nat. Gas Chem.* **2006**, *15* (3), 149−163.
(14) Chen, J.; Carlson, B. D.; Toops, T. J.; Li, Z.; Lance, M. J.; Karakalos, S. G.; Choi, J.-S.; Kyriakidou, E. A. Methane Combustion over Ni/$Ce_xZr_{1-x}O_2$ Catalysts: Impact of Ceria/Zirconia Ratio. *ChemCatChem.* **2020**, *12* (21), 5558−68.
(15) Ding, Y.; Jia, Y.; Jiang, M.; Guo, Y.; Guo, Y.; Wang, L.; Ke, Q.; Ngoc Ha, M.; Dai, S.; Zhan, W. Superior Catalytic Activity of Pd-Based Catalysts upon Tuning the Structure of the Ceria-Zirconia Support for Methane Combustion. *Chem. Eng. J.* **2021**, *416*, No. 129150.
(16) Toso, A.; Colussi, S.; Padigapaty, S.; de Leitenburg, C.; Trovarelli, A. High Stability and Activity of Solution Combustion Synthesized Pd-Based Catalysts for Methane Combustion in Presence of Water. *Appl. Catal., B* **2018**, *230*, 237−245.
(17) Ding, Y.; Wu, Q.; Lin, B.; Guo, Y.; Guo, Y.; Wang, Y.; Wang, L.; Zhan, W. Superior Catalytic Activity of a Pd Catalyst in Methane Combustion by Fine-Tuning the Phase of Ceria-Zirconia Support. *Appl. Catal., B* **2020**, *266*, No. 118631.
(18) Mueller, R.; Jossen, R.; Kammler, H. K.; Pratsinis, S. E.; Akhtar, M. K. Growth of Zirconia Particles Made by Flame Spray Pyrolysis. *AIChE J.* **2004**, *50* (12), 3085−3094.
(19) Wu, C.; Zhang, Y.; Yang, L.; Xiao, B.; Jiao, A.; Li, K.; Chen, T.; Huang, Z.; Lin, H. Flame Spray Pyrolysis Synthesis of WO_3 Sensing Materials: Effects of Flame Parameters on Particle Size Distribution and NO_2 Sensing Performance. *Langmuir* **2022**, *38* (50), 15506−15515.
(20) Laine, R. M.; Marchal, J.; Sun, H.; Pan, X. Q. A New $Y_3Al_5O_{12}$ Phase Produced by Liquid-Feed Flame Spray Pyrolysis (LF-FSP). *Adv. Mater.* **2005**, *17* (7), 830−833.
(21) Baker, C.; Kim, W.; Sanghera, J.; Goswami, R.; Villalobos, G.; Sadowski, B.; Aggarwal, I. Flame Spray Synthesis of Lu_2O_3 Nanoparticles. *Mater. Lett.* **2012**, *66* (1), 132−134.
(22) Zhang, Z.; Yu, J.; Zhang, J.; Ge, Q.; Xu, H.; Dallmann, F.; Dittmeyer, R.; Sun, J. Tailored Metastable Ce-Zr Oxides with Highly Distorted Lattice Oxygen for Accelerating Redox Cycles. *Chem. Sci.* **2018**, *9* (13), 3386−3394.
(23) Gunawan, C.; Lord, M. S.; Lovell, E.; Wong, R. J.; Jung, M. S.; Oscar, D.; Mann, R.; Amal, R. Oxygen-Vacancy Engineering of Cerium-Oxide Nanoparticles for Antioxidant Activity. *ACS Omega* **2019**, *4* (5), 9473−9479.
(24) Kim, M.; Laine, R. M. One-Step Synthesis of Core-Shell $(Ce_{0.7}Zr_{0.3}O_2)_x$ $(Al_2O_3)_{1-x}$ [$(Ce_{0.7}Zr_{0.3}O_2)$@Al_2O_3] Nanopowders via Liquid-Feed Flame Spray Pyrolysis (LF-FSP). *JACS.* **2009**, *131* (1), 9220−9229.
(25) Noriler, D.; Rosebrock, C. D.; Mädler, L.; Meier, H. F.; Fritsching, U. Influence of Atomization and Spray Parameters on the Flame Spray Process for Nanoparticle Production. *At. Sprays* **2014**, *24* (6), 495−524.
(26) Wang, N.; Li, S.; Zong, Y.; Yao, Q.; Zhang, Y. Flame Synthesis of Novel Ternary Nanocatalysts Pd/CeO_2-TiO_2 with Promotional Low-Temperature Catalytic Oxidation Properties. *Proc. Combust. Inst.* **2017**, *36* (1), 1029−1036.
(27) Zhao, F.; Li, S.; Chen, Y. Enhanced Thermal Stability and Oxygen Storage Capacity of Ceria-Zirconia Prepared by Flame Spray Pyrolysis under High Temperature. *J. Solid State Chem.* **2021**, *300* (March), No. 122216.
(28) Ravel, B.; Newville, M. ATHENA and ARTEMIS Interactive Graphical Data Analysis using IFEFFIT. *Phys. Scr.* **2005**, *T115*, 1007.
(29) Amorim, C.; Keane, M. A. Palladium Supported on Structured and Nonstructured Carbon: A Consideration of Pd Particle Size and the Nature of Reactive Hydrogen. *J. Colloid Interface Sci.* **2008**, *322* (1), 196−208.
(30) Aramendía, M. A.; Borau, V.; Jiménez, C.; Marinas, J. M.; Moreno, A. Comparative Measurements of the Dispersion of Pd Catalyst on SiO_2-$AlPO_4$ Support Using TEM and H_2 Chemisorption. *Colloids Surf. A Physicochem. Eng. Asp.* **1996**, *106* (2−3), 161−165.
(31) Cabañas, A.; Darr, J. A.; Lester, E.; Poliakoff, M. Continuous Hydrothermal Synthesis of Inorganic Materials in a Near-Critical Water Flow Reactor; the One-Step Synthesis of Nano-Particulate $Ce_{1-x}Zr_xO_2$ (x = 0−1) Solid Solutions. *J. Mater. Chem.* **2001**, *11* (2), 561−568.
(32) Yashima, M.; Sekikawa, T.; Sato, D.; Nakano, H.; Omoto, K. Crystal Structure and Oxide-Ion Diffusion of Nanocrystalline, Compositionally Homogeneous Ceria-Zirconia $Ce_{0.5}Zr_{0.5}O_2$ up to 1176 K. *Cryst. Growth Des.* **2013**, *13* (2), 829−837.
(33) Wang, C.; Sasmaz, E.; Wen, C.; Lauterbach, J. Pd Supported on SnO_2-MnO_x-CeO_2 Catalysts for Low Temperature CO Oxidation. *Catal. Today* **2015**, *258*, 481−486.
(34) Wang, C.; Wen, C.; Lauterbach, J.; Sasmaz, E. Superior Oxygen Transfer Ability of Pd/MnO_x-CeO_2 for Enhanced Low Temperature CO Oxidation Activity. *Appl. Catal., B* **2017**, *206*, 1−8.
(35) Baidya, T.; Bera, P.; Kröcher, O.; Safonova, O.; Abdala, P. M.; Gerke, B.; Pöttgen, R.; Priolkar, K. R.; Mandal, T. K. Understanding the Anomalous Behavior of Vegard's Law in $Ce_{1-x}M_xO_2$ (M = Sn and Ti; $0 < x \leq 0.5$) Solid Solutions. *Phys. Chem. Chem. Phys.* **2016**, *18* (20), 13974−13983.
(36) Sergent, N.; Lamonier, J. F.; Aboukaïs, A. Electron Paramagnetic Resonance in Combination with the Thermal Analysis, X-Ray Diffraction, and Raman Spectroscopy to Follow the Structural Properties of $Zr_xCe_{1-x}O_2$ Solid Systems and Precursors. *Chem. Mater.* **2000**, *12* (12), 3830−3835.
(37) Zhang, G.; Zhao, Z.; Liu, J.; Jiang, G.; Duan, A.; Zheng, J.; Chen, S.; Zhou, R. Three Dimensionally Ordered Macroporous $Ce_{1-x}Zr_xO_2$ Solid Solutions for Diesel Soot Combustion. *ChemComm.* **2010**, *46* (3), 457−459.
(38) Wang, C.; Ko, B.; Najimu, M.; Sasmaz, E. Application of Machine Learning and Laser-Induced Breakdown Spectroscopy to Flame Spray Pyrolysis for the Prediction of Catalyst Properties. *Chem. Mater.* **2023**, *35* (5), 1926−1934.
(39) Huang, X.; Zhang, K.; Peng, B.; Wang, G.; Muhler, M.; Wang, F. Ceria-Based Materials for Thermocatalytic and Photocatalytic Organic Synthesis. *ACS Cata.* **2021**, *11* (15), 9618−9678.
(40) Wang, S. P.; Zhang, T. Y.; Su, Y.; Wang, S. R.; Zhang, S. M.; Zhu, B. L.; Wu, S. H. An Investigation of Catalytic Activity for CO Oxidation of CuO/$Ce_xZr_{1-x}O_2$ Catalysts. *Catal. Lett.* **2008**, *121* (1−2), 70−76.
(41) Reddy, B. M.; Khan, A.; Lakshmanan, P.; Aouine, M.; Loridant, S.; Volta, J.-C. Structural Characterization of Nanosized CeO_2-SiO_2, CeO_2-TiO_2, and CeO_2-ZrO_2. *J. Phys. Chem. B* **2005**, *109*, 3355−3363.
(42) Li, L.; Chen, F.; Lu, J. Q.; Luo, M. F. Study of Defect Sites in $Ce_{1-x}M_xO_{2-\delta}$ (x = 0.2) Solid Solutions Using Raman Spectroscopy. *J. Phys.Chem. A* **2011**, *115* (27), 7972−7977.
(43) Yang, X.; Yang, L.; Lin, S.; Zhou, R. New Insight into the Doping Effect of Pr_2O_3 on the Structure-Activity Relationship of Pd/CeO_2-ZrO_2 Catalysts by Raman and XRD Rietveld Analysis. *J. Phys. Chem. C* **2015**, *119* (11), 6065−6074.
(44) Taniguchi, T.; Watanabe, T.; Sugiyama, N.; Subramani, A. K.; Wagata, H.; Matsushita, N.; Yoshimura, M. Identifying Defects in Ceria-Based Nanocrystals by UV Resonance Raman Spectroscopy. *J. Phys. Chem. C* **2009**, *113* (46), 19789−19793.
(45) Loridant, S. Raman Spectroscopy as a Powerful Tool to Characterize Ceria-Based Catalysts. *Catal. Today* **2021**, *373*, 98−111.
(46) Wu, Z.; Li, M.; Howe, J.; Meyer, H. M.; Overbury, S. H. Probing Defect Sites on CeO_2 Nanocrystals with Well-Defined Surface Planes by Raman Spectroscopy and O_2 Adsorption. *Langmuir* **2010**, *26* (21), 16595−16606.

https://doi.org/10.1021/acs.energyfuels.4c01888
Energy Fuels 2024, 38, 15571−15586

(47) Jiang, D.; Wan, G.; García-Vargas, C. E.; Li, L.; Pereira-Hernández, X. I.; Wang, C.; Wang, Y. Elucidation of the Active Sites in Single-Atom Pd_1/CeO_2 Catalysts for Low-Temperature CO Oxidation. *ACS Catal.* **2020**, *10* (19), 11356−11364.
(48) Chen, L. F.; González, G.; Wang, J. A.; Noreña, L. E.; Toledo, A.; Castillo, S.; Morán-Pineda, M. Surfactant-Controlled Synthesis of $Pd/Ce_{0.6}Zr_{0.4}O_2$ Catalyst for NO Reduction by CO with Excess Oxygen. *Appl. Surf. Sci.* **2005**, *243* (1−4), 319−328.
(49) Hu, Z.; Liu, X.; Meng, D.; Guo, Y.; Guo, Y.; Lu, G. Effect of Ceria Crystal Plane on the Physicochemical and Catalytic Properties of Pd/Ceria for CO and Propane Oxidation. *ACS Catal.* **2016**, *6* (4), 2265−2279.
(50) You, R.; Li, Z.; Cao, T.; Nan, B.; Si, R.; Huang, W. Synthesis in a Glovebox: Utilizing Surface Oxygen Vacancies to Enhance the Atomic Dispersion of Palladium on Ceria for Carbon Monoxide Oxidation and Propane Combustion. *ACS Appl. Nano Mater.* **2018**, *1* (9), 4988−4997.
(51) Wang, H. F.; Gong, X. Q.; Guo, Y. L.; Guo, Y.; Lu, G. Z.; Hu, P. A Model to Understand the Oxygen Vacancy Formation in Zr-Doped CeO_2: Electrostatic Interaction and Structural Relaxation. *J. Phys. Chem. C* **2009**, *113* (23), 10229−10232.
(52) Onn, T. M.; Arroyo-Ramirez, L.; Monai, M.; Oh, T. S.; Talati, M.; Fornasiero, P.; Gorte, R. J.; Khader, M. M. Modification of Pd/CeO_2 Catalyst by Atomic Layer Deposition of ZrO_2. *Appl. Catal., B* **2016**, *197*, 280−285.
(53) Łamacz, A.; Matus, K.; Liszka, B.; Silvestre-Albero, J.; Lafjah, M.; Dintzer, T.; Janowska, I. The Impact of Synthesis Method of CNT Supported $CeZrO_2$ and Ni-$CeZrO_2$ on Catalytic Activity in WGS Reaction. *Catal. Today* **2018**, *301*, 172−182.
(54) Shah, P. M.; Burnett, J. W. H.; Morgan, D. J.; Davies, T. E.; Taylor, S. H. Ceria−Zirconia Mixed Metal Oxides Prepared via Mechanochemical Grinding of Carbonates for the Total Oxidation of Propane and Naphthalene. *Catalysts* **2019**, *9* (5), 475.
(55) Danielis, M.; Betancourt, L. E.; Orozco, I.; Divins, N. J.; Llorca, J.; Rodríguez, J. A.; Senanayake, S. D.; Colussi, S.; Trovarelli, A. Methane Oxidation Activity and Nanoscale Characterization of Pd/CeO_2 Catalysts Prepared by Dry Milling Pd Acetate and Ceria. *Appl. Catal., B* **2021**, *282*, No. 119567.
(56) Shen, M.; Wang, J.; Shang, J.; An, Y.; Wang, J.; Wang, W. Modification Ceria-Zirconia Mixed Oxides by Doping Sr Using the Reversed Microemulsion for Improved Pd-Only Three-Way Catalytic Performance. *J. Phys. Chem. C* **2009**, *113* (4), 1543−1551.
(57) Wang, Q.; Li, G.; Zhao, B.; Zhou, R. The Effect of Nd on the Properties of Ceria-Zirconia Solid Solution and the Catalytic Performance of Its Supported Pd-Only Three-Way Catalyst for Gasoline Engine Exhaust Reduction. *J. Hazard. Mater.* **2011**, *189* (1−2), 150−157.
(58) Marrero-Jerez, J.; Larrondo, S.; Rodríguez-Castellón, E.; Núñez, P. TPR, XRD and XPS Characterization of Ceria-Based Materials Synthesized by Freeze-Drying Precursor Method. *Ceram. Int.* **2014**, *40* (5), 6807−6814.
(59) Ciuparu, D.; Ensuque, A.; Bozon-Verduraz, F. Pd Catalysts Supported on MgO, ZrO_2 or MgO-ZrO_2: Preparation, Characterization and Study in Hexane Conversion. *Appl. Catal. A Gen.* **2007**, *326* (2), 130−142.
(60) Ranga, C.; Alexiadis, V. I.; Lauwaert, J.; Lødeng, R.; Thybaut, J. W. Effect of Co Incorporation and Support Selection on Deoxygenation Selectivity and Stability of (Co)Mo Catalysts in Anisole HDO. *Appl. Catal. A Gen.* **2019**, *571*, 61−70.
(61) Sadykov, V.; Mezentseva, N. V.; Alikina, G. M.; Lukashevich, A. I.; Borchert, Y. V.; Kuznetsova, T. G.; Ivanov, V. P.; Trukhan, S. N.; Paukshtis, E. A.; Muzykantov, V. S.; Kuznetsov, V. L.; Rogov, V. A.; Ross, J. R. H.; Kemnitz, E.; Mirodatos, C. Pt-Supported Nanocrystalline Ceria-Zirconia Doped with La, Pr or Gd: Factors Controlling Syngas Generation in Partial Oxidation/Autothermal Reforming of Methane or Oxygenates. *Solid State Phenom.* **2007**, *128*, 239−248.
(62) Li, J.; Liu, X.; Zhan, W.; Guo, Y.; Guo, Y.; Lu, G. Preparation of High Oxygen Storage Capacity and Thermally Stable Ceria-Zirconia Solid Solution. *Catal. Sci. Technol.* **2016**, *6* (3), 897−907.
(63) Yarar, M.; Bouziani, A.; Uner, D. Pd as a Reduction Promoter for TiO_2: Oxygen and Hydrogen Transport at 2D and 3D Pd Interfaces with TiO_2 Monitored by TPR, Operando 1H NMR and CO Oxidation Studies. *Catal. Commun.* **2023**, *174*, No. 106580.
(64) Du, J.; Li, H.; Wang, C.; Zhang, A.; Zhao, Y.; Luo, Y. Improved Catalytic Activity over P-Doped Ceria-Zirconia-Alumina Supported Palladium Catalysts for Methane Oxidation. *Catal. Commun.* **2020**, *141* (April), No. 106012.
(65) Hoflund, G. B.; Hagelin, H. A. E.; Weaver, J. F.; Salaita, G. N. ELS and XPS Study of Pd/PdO Methane Oxidation Catalysts. *Appl. Surf. Sci.* **2003**, *205* (1−4), 102−112.
(66) Li, G.; Wang, Q.; Zhao, B.; Shen, M.; Zhou, R. Effect of Iron Doping into CeO_2-ZrO_2 on the Properties and Catalytic Behaviour of Pd-Only Three-Way Catalyst for Automotive Emission Control. *J. Hazard. Mater.* **2011**, *186* (1), 911−920.
(67) Lupescu, J. A.; Schwank, J. W.; Fisher, G. B.; Chen, X.; Peczonczyk, S. L.; Drews, A. R. Pd Model Catalysts: Effect of Aging Duration on Lean Redispersion. *Appl. Catal., B* **2016**, *185*, 189−202.
(68) Sasmaz, E.; Wang, C.; Lance, M. J.; Lauterbach, J. In Situ Spectroscopic Investigation of a Pd Local Structure over Pd/CeO_2 and Pd/MnO_x-CeO_2 during CO Oxidation. *J. Mater. Chem. A* **2017**, *5* (25), 12998−13008.
(69) Liang, F.; Zhu, H.; Qin, Z.; Wang, G.; Wang, J. Effects of CO_2 on the Stability of Pd/CeO_2-TiO_2 Catalyst for Low-Temperature CO Oxidation. *Catal. Commun.* **2009**, *10* (5), 737−740.
(70) Zhu, H.; Qin, Z.; Shan, W.; Shen, W.; Wang, J. Pd/CeO_2-TiO_2 Catalyst for CO Oxidation at Low Temperature: A TPR Study with H2 and CO as Reducing Agents. *J. Catal.* **2004**, *225* (2), 267−277.
(71) Spezzati, G.; Su, Y.; Hofmann, J. P.; Benavidez, A. D.; DeLaRiva, A. T.; McCabe, J.; Datye, A. K.; Hensen, E. J. M. Atomically Dispersed Pd-O Species on CeO_2 (111) as Highly Active Sites for Low-Temperature CO Oxidation. *ACS Catal.* **2017**, *7* (10), 6887−6891.
(72) Delannoy, L.; Giorgio, S.; Mattei, J. G.; Henry, C. R.; ElKolli, N.; Méthivier, C.; Louis, C. Surface Segregation of Pd from TiO_2-Supported Aupd Nanoalloys under Co Oxidation Conditions Observed Insitu by Etem and Drifts. *ChemCatChem.* **2013**, *5* (9), 2707−2716.
(73) Boronin, A. I.; Slavinskaya, E. M.; Danilova, I. G.; Gulyaev, R. V.; Amosov, Y. I.; Kuznetsov, P. A.; Polukhina, I. A.; Koscheev, S. V.; Zaikovskii, V. I.; Noskov, A. S. Investigation of Palladium Interaction with Cerium Oxide and Its State in Catalysts for Low-Temperature CO Oxidation. *Catal. Today* **2009**, *144* (3−4), 201−211.
(74) Muravev, V.; Spezzati, G.; Su, Y. Q.; Parastaev, A.; Chiang, F. K.; Longo, A.; Escudero, C.; Kosinov, N.; Hensen, E. J. M. Interface Dynamics of Pd−CeO_2 Single-Atom Catalysts during CO Oxidation. *Nat. Catal.* **2021**, *4* (6), 469−478.
(75) Priolkar, K. R.; Bera, P.; Sarode, P. R.; Hegde, M. S.; Emura, S.; Kumashiro, R.; Lalla, N. P. Formation of $Ce_{1-x}Pd_xO_{2-\delta}$ Solid Solution in Combustion-Synthesized Pd/CeO_2 Catalyst: XRD, XPS, and EXAFS Investigation. *Chem. Mater.* **2002**, *14* (5), 2120−2128.
(76) Yang, W.; Kim, M. Y.; Polo-Garzon, F.; Gong, J.; Jiang, X.; Huang, Z.; Chi, M.; Yu, X.; Wang, X.; Guo, Y.; Wu, Z. CH_4 Combustion over a Commercial Pd/CeO_2-ZrO_2 Three-Way Catalyst: Impact of Thermal Aging and Sulfur Exposure. *J. Chem. Eng.* **2023**, *451*, 138930.
(77) Li, J.; Liu, X.; Zhan, W.; Guo, Y.; Guo, Y.; Lu, G. Preparation of High Oxygen Storage Capacity and Thermally Stable Ceria-Zirconia Solid Solution. *Catal. Sci. Technol.* **2016**, *6* (3), 897−907.
(78) Colussi, S.; Fornasiero, P.; Trovarelli, A. Structure-Activity Relationship in Pd/CeO_2 Methane Oxidation Catalysts. *Chinese Journal of Catalysis* **2020**, *41* (6), 938−950.
(79) Lott, P.; Dolcet, P.; Casapu, M.; Grunwaldt, J. D.; Deutschmann, O. The Effect of Prereduction on the Performance of Pd/Al_2O_3 and Pd/CeO_2 Catalysts during Methane Oxidation. *Ind. Eng. Chem. Res.* **2019**, *58* (28), 12561−12570.
(80) Cui, Y.; Zhu Chen, J.; Peng, B.; Kovarik, L.; Devaraj, A.; Li, Z.; Ma, T.; Wang, Y.; Szanyi, J.; Miller, J. T.; Wang, Y.; Gao, F. Onset of High Methane Combustion Rates over Supported Palladium

https://doi.org/10.1021/acs.energyfuels.4c01888
Energy Fuels 2024, 38, 15571−15586

Catalysts: From Isolated Pd Cations to PdO Nanoparticles. *JACS Au* **2021**, *1* (4), 396−408.

https://doi.org/10.1021/acs.energyfuels.4c01888
Energy Fuels 2024, 38, 15571−15586